Title

Mechanism of improved electrochemical performance of anode-supported solid oxide fuel cells by mesostructural modification of electrode–electrolyte interface

Authors

*Haewon Seo[1], Masashi Kishimoto[2], Taishi Nakagawa[1], Hiroshi Iwai[2], Hideo Yoshida[1]

Institutions

1. Department of Aeronautics and Astronautics, Kyoto University, Nishikyo-ku, Kyoto 615-8540, Japan

2. Department of Mechanical Engineering and Science, Kyoto University, Nishikyo-ku, Kyoto 615-8540, Japan

***Corresponding author**

E-mail: seo.haewon.52c@st.kyoto-u.ac.jp

Tel & Fax: +81-75-383-3652

Abstract

The mechanism whereby structural modification on the mesoscale order (10–100 μm) improves the electrochemical performance of anode-supported solid oxide fuel cells (SOFCs) is elucidated. After preparing two types of anode-supported SOFC having different electrode–electrolyte interfacial areas, we carry out their structural analyses and electrochemical characterization. Next, we develop a two-dimensional (2D) numerical model in which the structures of the cells are implemented and then verify its validity by comparing experimental and simulation results. It is found that the structural features in the mesoscale-modified cell, such as interfacial area enlargement and thickness inhomogeneity, cause nonuniform distributions of physicochemical quantities that contribute to electrochemical reactions. Consequently, the decreases in the ohmic and activation overpotentials of the mesoscale-modified cell relative to the flat cell are respectively larger and smaller than those estimated under the assumptions that the ionic and charge-transfer current densities are uniformly distributed in a cell. Moreover, the ionic current density distribution has a strong nonuniformity at a high current density, leading to a large relative decrease in ohmic loss. Furthermore, the cell overpotential is more reduced at a higher current density; thus, the mesostructural modification of anode-supported SOFCs can lead to a higher cell performance.

Keywords

Anode-supported solid oxide fuel cell; Electrode–electrolyte interface; Mesoscale structural modification; Numerical analysis; Overpotential; Thickness inhomogeneity

1. Introduction

Solid oxide fuel cells (SOFCs) are attracting widespread attention owing to their high energy conversion and fuel diversity. To minimize the size of SOFC systems and thereby reduce their manufacturing costs and heat capacity, it is necessary to increase the volumetric power density of individual cells. For this purpose, researchers have been focusing on the design of a cell structure on the mesoscale order (10–100 μm) to enlarge the electrode–electrolyte interfacial area [1–10]. This is because the electrochemical reactions in porous electrodes actively occur at the reaction sites distributed in a very thin region with a thickness of around 5–20 μm near the electrode–electrolyte interface [11–15].

Owing to the recent advances in manufacturing technology, the mesostructural modification of SOFCs has been realized, resulting in markedly enhanced cell performance [1,3–10,16]. For instance, we achieved an increase of 14% in the electrode–electrolyte interfacial area of an anode-supported SOFC relative to a flat cell by forming anode ridge structures on a surface of a flat anode disk using a microextrusion printing technique [7]. Through electrochemical impedance spectroscopy, it was confirmed that the relative decreases in the ohmic and activation resistances were 42–45 and 54–59%, respectively, under the open-circuit voltage condition at 600–700 °C. More recently, Shin et al. [8] have fabricated an anode-supported SOFC where the electrode–electrolyte interfacial area was enlarged by about 23% compared with that of a flat cell by micropatterning through polymer-to-ceramic transformation. They reported that the ohmic and polarization resistances in the cell obtained at a terminal voltage of 0.75 V at 500–600 °C were 29–52 and 15–23% lower than those in the flat cell, respectively. Although it has been demonstrated that mesostructural modification improves cell performance, there is no consistency in the relationships between the relative increase in interfacial area and the relative decrease in cell resistance among the existing experimental results [1,3–10,16]. This is because the electrochemical performance of SOFCs is affected by multiple factors such as the cell structure, operating conditions, and materials for the cell components. Accordingly, numerical

simulation in which these factors are appropriately considered is expected to provide important clues for understanding the effect of mesostructural modification.

Thus far, various numerical models have been developed to investigate the effect of the mesostructural modification of SOFCs on improving the cell performance [1,6,17–23]. For example, Konno et al. [1,18] analyzed the distributions of physicochemical quantities within mesoscale-modified cells during power generation and thereby found that introducing mesoscale corrugated structures into the electrode–electrolyte interface reduced both ohmic and activation overpotentials. Moreover, they clarified that its effect became more prominent with increasing electrode–electrolyte interfacial area, particularly in a cell having a thin electrolyte such as an anode-supported SOFC. It has also been reported that the electrode microstructure [6,18,22] and the geometrical shape of the electrode–electrolyte interface [17,19–21,23] determine the effect of mesostructural modification. Despite these key findings, a detailed mechanism whereby mesostructural modification improves cell performance has not yet been clarified. In addition, a lack of understanding regarding the improvement in cell performance by mesostructural modification in quantitative terms still remains [1,20]. For example, according to the literature [1], the current density at 0.5 V at 800 °C increased from 42.2 to 52.8 mA cm^{-2} in the measurement, whereas it increased from 259 to 287 mA cm^{-2} in the simulation. These quantitative discrepancies between the electrochemical characteristics of each cell obtained from the experiment and simulation led to a mismatch of the increases in the electrochemical performance of a mesoscale-modified cell relative to a flat cell. This is because the cell structures at multiple scales—the electrode microstructure, cell component thickness, and geometric shape of the electrode–electrolyte interface—used in the electrochemical testing were not properly considered in the numerical model. Thus, a numerical model with high validity must first be constructed to clarify the aforementioned unresolved issues.

Herein, the mechanism whereby mesostructural modification improves the electrochemical performance of anode-supported SOFCs is elucidated. After preparing two types of anode-supported

SOFC having different electrode–electrolyte interfacial areas, we carry out their structural analyses and electrochemical characterization. Next, we develop a two-dimensional (2D) numerical model in which the structures of the tested cells are implemented and then verify its validity by comparing experimental and simulation results. Subsequently, changes in the overpotential components of the mesoscale-modified cell relative to the flat cell are quantitatively evaluated. Through analyzing the distributions of physicochemical quantities that contribute to the electrochemical reactions inside the cells, the mechanism of the improved cell performance by mesostructural modification is discussed on the basis of the energy losses attributed to such quantities. Finally, the effect of mesostructural modification at various current densities is investigated.

2. Experimental

2.1. Cell preparation

Two types of 20-mm-diameter anode-supported button SOFC having different electrode–electrolyte interfacial areas, a flat cell (FLAT) as a reference and a mesoscale-modified cell (MESO), were prepared. An anode disk and anode ridge structures were prepared by tape casting and microextrusion printing, respectively, using an identically prepared homogeneous NiO (FUJIFILM Wako Pure Chemical Corp., Japan)–$(Y_2O_3)_{0.08}(ZrO_2)_{0.92}$ (YSZ) (TZ-8Y, Tosoh Corp., Japan) anode slurry (NiO:YSZ = 60:40 wt%). The anode ridge structures were uniformly formed by extruding the anode slurry onto the surface of a flat green disk, and their average width and height were measured to be 140.6 and 35.4 μm, respectively. Thereafter, the NiO–YSZ anode was presintered at 1200 °C for 2 h. A YSZ electrolyte thin film was deposited onto the anode surface by spin coating, which was followed by sintering at 1350 °C for 5 h. A $Gd_{0.1}Ce_{0.9}O_{1.95}$ (GDC) (GDC-10(AU), Shin-Etsu Astech Co., Ltd., Japan) barrier layer and a $La_{0.6}Sr_{0.4}Co_{0.2}Fe_{0.8}O_{3-\delta}$ (LSCF) (LSCF-6428-N, Kceracell Co., Ltd., Korea) cathode were formed with laboratory-made screen-printable inks, which were sequentially sintered at 1250 °C for 2 h and 950 °C for 5 h. The apparent surface area of the LSCF cathode was about 0.785 cm^2. The cell preparation is described in more detail in our previous works [24,25].

2.2. Performance evaluation

The electrochemical performance of the cells was evaluated at 700 °C. Each cell was held with two alumina tubes to which sealing glass rings were attached. A platinum mesh was used as a current collector for both electrodes. The cell temperature was controlled using an electric furnace. Mixture gases of 97% H_2–3% H_2O and 21% O_2–79% N_2 were supplied to the anode and cathode, respectively, whose total flow rate was 100 sccm at both electrodes. A Solartron 1470E potentio/galvanostat electrochemical interface (Solartron Analytical, UK) was used to measure the current–voltage (*i*–*V*)

characteristics of the cells. More details can be found elsewhere [7].

2.3. Structure analysis

Prior to structural analysis, the cells were cooled in a reducing atmosphere after the electrochemical testing and then impregnated with epoxy resin (EpoFix, Struers, Denmark) under a pressure of 34 Pa for 10 min. For mesostructural analysis, the cured samples were cut and polished to observe their cross sections by scanning electron microscopy (SEM) (Miniscope TM3000, Hitachi High-Tech Corp., Japan) [7]. For microstructural analysis, a small piece of the cured sample was painted with a commercial silver paste (Ted Pella, Inc., USA) and then coated with osmium under a pressure of 8–10 Pa for 10 s. The three-dimensional (3D) microstructures of both electrodes were imaged using an NVision 40 (Carl Zeiss AG, Germany) focused ion beam (FIB) SEM system. An in-lens secondary electron detector and a standard secondary electron detector with an acceleration voltage of 2.0 kV were used to distinguish the solid phases in the Ni–YSZ anode and LSCF cathode, respectively, in SEM images. Sliced SEM images were aligned and segmented into three and two phases for the Ni–YSZ anode and LSCF cathode, respectively, and then reconstructed to quantify microstructural parameters. The phase volume fraction, particle and pore sizes, tortuosity factor, surface-to-volume ratio, double-phase boundary (DPB) density, and triple-phase boundary (TPB) density were quantified using a commercial 3D visualization and analysis software application (Avizo, Thermo Fisher Scientific Inc., USA) and an in-house code. More details of the image processing procedures and quantification methods can be found elsewhere [26–30].

3. Numerical simulation

3.1. Numerical model

We developed a steady-state 2D numerical model in which the structures of the cells after the electrochemical testing were implemented. **Figure 1(a)** shows cross-sectional SEM images of the tested cells [24]. The green, yellow, white, and gray areas in the SEM images correspond to the Ni–YSZ anode, YSZ electrolyte, GDC barrier layer, and LSCF cathode; their average thicknesses in the flat cell were measured to be about 450, 8.0, 6.0, and 36 μm, respectively. On the other hand, the thicknesses of the layers in the mesoscale-modified cell could not be defined because of their inhomogeneity. Therefore, we identified each layer from its cross-sectional SEM image and then obtained geometric shape data using Avizo software. The average interval between two adjacent anode ridge structures after sintering at 1350 °C, which was measured to be about 202 μm using a 3D laser confocal scanning microscope (LEXT OLS4000, Olympus Corp., Japan), was set as a single repeating unit L. The interfacial area enlargement factor α—the ratio of the contact area between the electrode and electrolyte of the mesoscale-modified cell to that of the flat cell—was calculated to be about 1.14 for the anode–electrolyte interface and about 1.08 for the cathode–electrolyte interface. Details of the calculation of the interfacial area enlargement are described in Ref. [7]. Thereby, the average interfacial area enlargement factor was about 1.11 $\left(=\frac{\alpha_{\mathrm{A\text{-}E}}L+\alpha_{\mathrm{C\text{-}E}}L}{L+L}\right)$. Note that the ratio of the cross-sectional area of the YSZ/GDC bilayer in the mesoscale-modified cell to that in the flat cell was calculated to be 1.14. By taking these values into consideration, the calculation domains of each cell were designated as the areas surrounded by the blue solid lines in **Fig. 1(b)**. Note that x and y in the orthogonal coordinate system shown in **Fig. 1(b)** were defined as the cell width and thickness directions, respectively. To reduce the computational load, the calculation grid dimensions were set at 1×1 μm^2 in the region where y is greater than 420 μm and 1×5 μm^2 elsewhere. Taking into account the porosity of the GDC barrier layer (*ca*. 50%) and the ionic conductivity of GDC [31,32], we included the barrier layer thickness in the electrolyte thickness as an equivalent YSZ thickness [25]. The electrode

microstructures were assumed to be homogeneous in the entire region of each electrode. **Figures 1(c)** and **1(d)** show the 3D reconstructed structures of the electrodes, whose volumes were 14.86 × 21.05 × 12.96 and 9.74 × 11.45 × 9.75 μm^3 for the Ni–YSZ anode and LSCF cathode, respectively [25]. The microstructural parameters quantified from the results of FIB-SEM analysis summarized in **Table 1** were used in the numerical simulation.

Table 1 Microstructural parameters of electrodes of tested cell [25].

Parameter	Anode			Cathode	
	Ni	YSZ	Pores	LSCF	Pores
Volume fraction/%	33.0	38.9	28.1	54.6	45.4
Particle/pore size/μm	1.50	1.12	0.955	0.218	0.211
Tortuosity factor/–	3.43	2.33	7.89	2.64	1.79
Surface-to-volume ratio/$\mu m^2\ \mu m^{-3}$	4.02	5.37	5.97	11.1	13.4
DPB density/$\mu m^2\ \mu m^{-3}$	–			6.07	
TPB density/$\mu m\ \mu m^{-3}$	2.29			–	

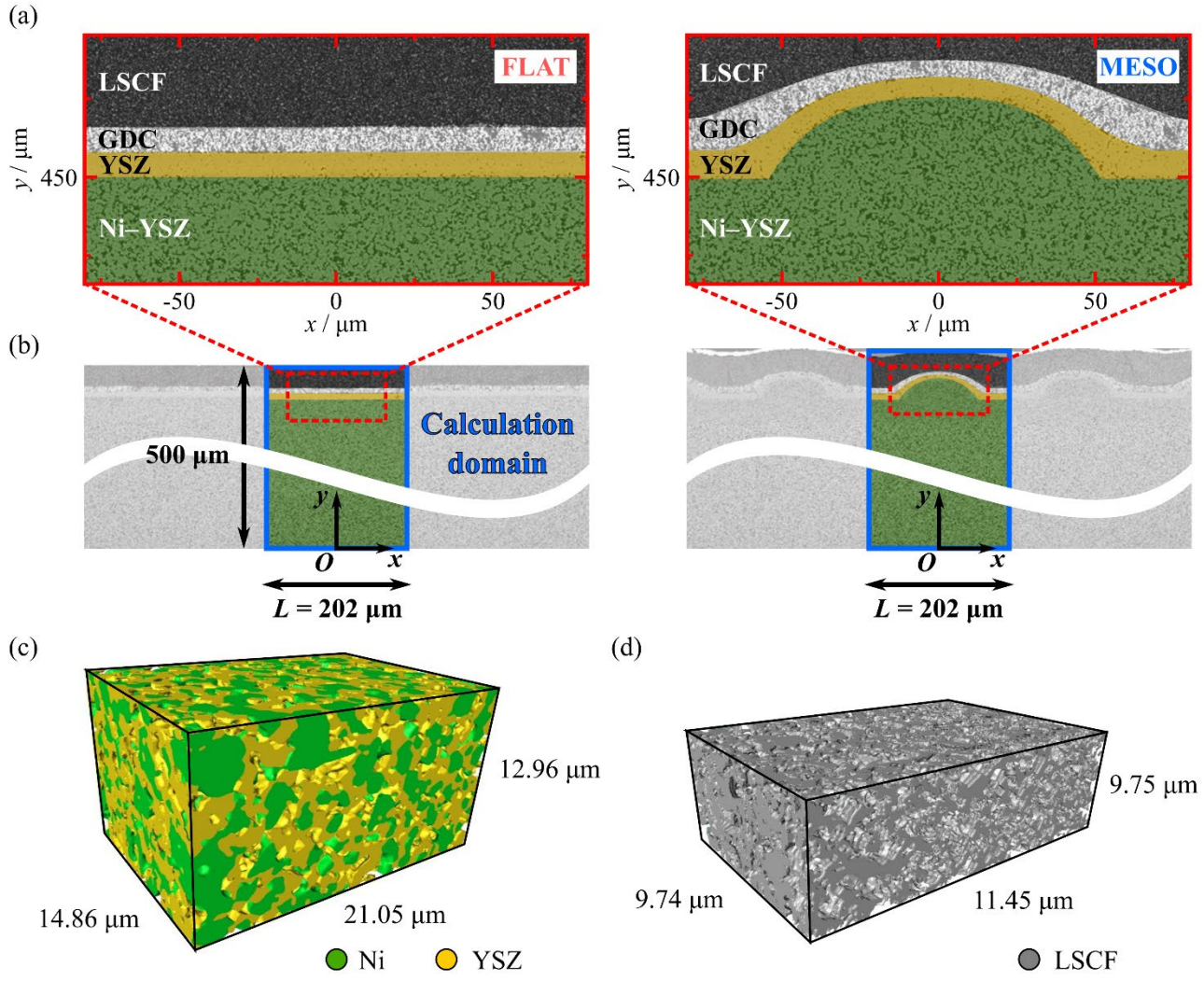

Fig. 1 (a) Cross-sectional SEM images [24] and (b) calculation domains of cells, and 3D reconstructed structures of (c) Ni–YSZ anode and (d) LSCF cathode.

3.2. Governing equations

The conservation of electrons and that of oxide ions are expressed as

$$\nabla\cdot\left(\frac{\sigma_{\mathrm{e}^-}^{\mathrm{eff}}}{F}\nabla\bar{\mu}_{\mathrm{e}^-}\right)=-i_{\mathrm{ct}} \tag{1}$$

$$\nabla\cdot\left(\frac{\sigma_{\mathrm{O}^{2-}}^{\mathrm{eff}}}{2F}\nabla\bar{\mu}_{\mathrm{O}^{2-}}\right)=i_{\mathrm{ct}}, \tag{2}$$

where $\sigma_{e^-}^{eff}$ and $\sigma_{O^{2-}}^{eff}$ are respectively the effective electronic and ionic conductivities. Moreover, F is the Faraday constant, $\bar{\mu}_{e^-}$ and $\bar{\mu}_{O^{2-}}$ are respectively the electrochemical potentials of the electrons and oxide ions, and i_{ct} is the charge-transfer current density associated with the electrochemical reactions in the electrodes. In this numerical model, LSCF, Ni, and YSZ were considered as mixed ion–electron, pure electron, and pure ion conductors, respectively.

Gas diffusion in the electrodes is expressed by the dusty-gas model [33–36] as

$$\nabla \cdot N_i = \dot{s}_i \tag{3}$$

$$\frac{N_i}{D_{i,K}^{eff}} + \sum_{j=1, j\neq i}^{n} \frac{X_j N_i - X_i N_j}{D_{ij}^{eff}} = -\frac{P_t}{RT}\nabla X_i - \frac{X_i}{RT}\left(1 + \frac{K P_t}{\mu D_{i,K}^{eff}}\right)\nabla P_t. \tag{4}$$

Here, N_i and X_i represent the molar flux and molar fraction, respectively, and $\dot{s}_i$ is the sink/source term associated with the electrochemical reaction, where

$$\dot{s}_{H_2} = -\frac{i_{ct}}{2F},\ \dot{s}_{H_2O} = \frac{i_{ct}}{2F},\ \dot{s}_{O_2} = -\frac{i_{ct}}{4F},\ \dot{s}_{N_2} = 0. \tag{5}$$

Also, $D_{i,K}^{eff}$ and D_{ij}^{eff} are the effective Knudsen and effective molecular diffusivities, and P_t, K, and μ are the total pressure, permeability, and mixture viscosity, respectively.

The effective conductivities and gas diffusivities were evaluated by modifying the bulk transport coefficients using the ratio of the volume fraction V_i to the tortuosity factor τ_i as

$$\Gamma_i^{eff} = \frac{V_i}{\tau_i}\Gamma_i \ \ (\Gamma_i \equiv \sigma_{e^-}, \sigma_{O^{2-}}, D_{i,K}, D_{ij}). \tag{6}$$

The empirical formulas used for the bulk conductivities and bulk gas diffusivities were [37–41]

$$\log \sigma_{e^-,\mathrm{LSCF}} = -0.0095 \left(\log \frac{P_{O_2}}{10^5}\right)^2 - 0.0011 \log \frac{P_{O_2}}{10^5} + 4.8152 \quad (7)$$

$$\sigma_{e^-,\mathrm{Ni}} = 3.27 \times 10^6 - 1065.3T \quad (8)$$

$$\sigma_{O^{2-},\mathrm{LSCF}} = \frac{8F^2 \widetilde{D}}{RTV_m} \frac{\partial \delta}{\partial \ln P_{O_2}} \quad (9)$$

$$\sigma_{O^{2-},\mathrm{YSZ}} = 3.40 \times 10^4 \exp\left(-\frac{8.60\times10^4}{RT}\right) \quad (10)$$

$$D_{i,\mathrm{K}} = \frac{d_{\mathrm{pore}}}{3} \sqrt{\frac{8RT}{10^{-3}\pi M_i}} \quad (11)$$

$$D_{ij} = \frac{0.01013T^{1.75}\left(M_i^{-1}+M_j^{-1}\right)^{1/2}}{P_t\left[\left(\sum v_i \times 10^6\right)^{1/3}+\left(\sum v_j \times 10^6\right)^{1/3}\right]^2}. \quad (12)$$

Here, $\widetilde{D}$ is the chemical diffusion coefficient, which is expressed as [37]

$$\log \widetilde{D} = -0.1882 \left(\log \frac{P_{O_2}}{10^5}\right)^2 - 0.2490 \log \frac{P_{O_2}}{10^5} - 9.7676. \quad (13)$$

Also, V_m is the perovskite molar volume and was set at 35.17 cm^3 mol^{-1} [42] in this work. δ is the oxygen nonstoichiometry, d_{pore} is the mean pore diameter, M_i is the molecular mass, and $\sum v_i$ is the molecular diffusion volume. The permeability of the porous electrodes was evaluated using the following equation proposed by Kishimoto et al. [27]:

$$K = \frac{V_{\mathrm{pore}}}{6\tau_{\mathrm{pore}}(S/V)^2_{\mathrm{pore}}}. \quad (14)$$

Here, $(S/V)_{\mathrm{pore}}$ indicates the surface-to-volume ratio of the pore phase.

We assumed that electrochemical reactions occur at TPBs in the Ni–YSZ anode and at DPBs in the LSCF cathode, which are described with nonlinear Butler–Volmer-type equations [38,43] as

$$i_{\mathrm{ct,ano}} = i_{0,\mathrm{TPB,ano}} l_{\mathrm{TPB,ano}} \left[\exp\left(\frac{2F}{RT}\eta_{\mathrm{act,ano}}\right) - \exp\left(-\frac{F}{RT}\eta_{\mathrm{act,ano}}\right)\right] \quad (15)$$

$$i_{\mathrm{ct,cat}} = i_{0,\mathrm{DPB,cat}} A_{\mathrm{DPB,cat}} \left[\exp\left(\frac{1.2F}{RT}\eta_{\mathrm{act,cat}}\right) - \exp\left(-\frac{F}{RT}\eta_{\mathrm{act,cat}}\right)\right]. \quad (16)$$

Here, i_0 indicates the exchange current density and is given by [44,45]

$$i_{0,\mathrm{TPB,ano}} = 1.30 \times 10^{-3} P_{\mathrm{H_2}}^{0.11} P_{\mathrm{H_2O}}^{0.67} \exp\left(-\frac{8.49\times10^4}{RT}\right) \quad (17)$$

$$i_{0,\mathrm{DPB,cat}} = 1.47 \times 10^{6} P_{\mathrm{O_2}}^{0.2} \exp\left(-\frac{8.59\times10^4}{RT}\right). \quad (18)$$

Also, $l_{\mathrm{TPB,ano}}$ and $A_{\mathrm{DPB,cat}}$ respectively represent the TPB and DPB densities, for which the quantified values obtained from the results of microstructural analysis shown in **Table 1** are used. η_{act} is the activation overpotential and is defined as

$$\eta_{\mathrm{act,ano}} = -\frac{1}{2F}\left(2\bar{\mu}_{\mathrm{e^-}} - \bar{\mu}_{\mathrm{O^{2-}}} + \Delta G_0 - RT \ln \frac{P_{\mathrm{H_2}}^{\mathrm{bulk}}}{P_{\mathrm{H_2O}}^{\mathrm{bulk}}}\right) - \eta_{\mathrm{con,ano}} \quad (19)$$

$$\eta_{\mathrm{act,cat}} = -\frac{1}{2F}\left(2\bar{\mu}_{\mathrm{e^-}} - \bar{\mu}_{\mathrm{O^{2-}}} + \frac{RT}{2} \ln P_{\mathrm{O_2}}^{\mathrm{bulk}}\right) - \eta_{\mathrm{con,cat}}. \quad (20)$$

Here, ΔG_0 indicates the standard Gibbs free energy change associated with the hydrogen oxidation reaction and η_{con} is the concentration overpotential and is defined as

$$\eta_{\mathrm{con,ano}} = \frac{RT}{2F} \ln\left(\frac{P_{\mathrm{H_2}}^{\mathrm{bulk}}}{P_{\mathrm{H_2}}} \frac{P_{\mathrm{H_2O}}}{P_{\mathrm{H_2O}}^{\mathrm{bulk}}}\right) \quad (21)$$

$$\eta_{\mathrm{con,cat}} = \frac{RT}{4F} \ln\left(\frac{P_{\mathrm{O_2}}}{P_{\mathrm{O_2}}^{\mathrm{bulk}}}\right). \quad (22)$$

3.3. Boundary conditions

The boundary conditions on the electrode surfaces are summarized in **Table 2** (t_{cell} indicates the cell thickness). The cell temperature was assumed to be constant and uniform in the entire cell and set at 700 °C. Mixture gases of 97% H_2–3% H_2O and 21% O_2–79% N_2 were supplied to the anode and cathode surfaces, respectively. The total pressure on the surfaces of both electrodes was set at 1 atm. The electrochemical potential of the electrons was set as the product of the terminal voltage V_{T} and the Faraday constant F at the anode surface and zero at the cathode surface [46]. The gradients of the electrochemical potentials of the oxide ions at the electrode surfaces were set as zero. Symmetric boundary conditions were set at the side boundaries $x = \pm\frac{L}{2}$ for all variables.

Table 2 Boundary conditions on electrode surfaces.

Variable	Anode surface ($y = 0$)	Cathode surface ($y = t_{\mathrm{cell}}$)
H_2 partial pressure	$P_{\mathrm{H_2}}(x,0) = P_{\mathrm{H_2}}^{\mathrm{bulk}}$	–
H_2O partial pressure	$P_{\mathrm{H_2O}}(x,0) = P_{\mathrm{H_2O}}^{\mathrm{bulk}}$	–
O_2 partial pressure	–	$P_{\mathrm{O_2}}(x,t_{\mathrm{cell}}) = P_{\mathrm{O_2}}^{\mathrm{bulk}}$
N_2 partial pressure	–	$P_{\mathrm{N_2}}(x,t_{\mathrm{cell}}) = P_{\mathrm{N_2}}^{\mathrm{bulk}}$
Electrochemical potential of electrons	$\bar{\mu}_{\mathrm{e^-}}(x,0) = FV_{\mathrm{T}}$	$\bar{\mu}_{\mathrm{e^-}}(x,t_{\mathrm{cell}}) = 0$
Electrochemical potential of oxide ions	$\frac{\partial \bar{\mu}_{\mathrm{O^{2-}}}}{\partial y}(x,0) = 0$	$\frac{\partial \bar{\mu}_{\mathrm{O^{2-}}}}{\partial y}(x,t_{\mathrm{cell}}) = 0$

3.4. Overpotential evaluation

To quantitatively understand the improved electrochemical performance of anode-supported SOFCs by the mesostructural modification of the electrode–electrolyte interface, we introduced average ohmic, activation, and concentration overpotentials in the cells [18,47]. In the previous work [18], the local ohmic loss attributed to oxide ion transport was calculated on the basis of the potential difference between an arbitrary point in an electrode and a reference point at the electrode–electrolyte

interface. However, this calculation method cannot be applied to a mesoscale-modified cell because a definite reference potential cannot be specified [18]. In this work, therefore, we propose another calculation method for the average ohmic loss in the cell; the average ohmic loss $\bar{\eta}_{\mathrm{ohm}}$ was calculated by averaging the total Joule heating with the total current as

$$\bar{\eta}_{\mathrm{ohm}} = \frac{\iint \sigma^{-1} i^2 dxdy}{\iint i_{\mathrm{ct}} dxdy}, \tag{23}$$

where i is the local current density.

The average activation overpotential $\bar{\eta}_{\mathrm{act}}$ and average concentration overpotential $\bar{\eta}_{\mathrm{con}}$ in each electrode were calculated by averaging the total energy loss with the total current as [18,47]

$$\bar{\eta}_{\mathrm{act}} = \frac{\iint \eta_{\mathrm{act}} i_{\mathrm{ct}} dxdy}{\iint i_{\mathrm{ct}} dxdy} \tag{24}$$

$$\bar{\eta}_{\mathrm{con}} = \frac{\iint \eta_{\mathrm{con}} i_{\mathrm{ct}} dxdy}{\iint i_{\mathrm{ct}} dxdy}. \tag{25}$$

4. Results and discussion

4.1. Model validation

Figure 2 shows the *i–V* and current–power (*i–P*) curves of the cells obtained from the experiment and numerical simulation at 700 °C. Note that the average current density was defined as the total current divided by the apparent electrode area. It was found that the electrochemical performance of the mesoscale-modified cell is improved compared with that of the flat cell under the same operating conditions in both the experimental and numerical results. This indicates that the cell overpotential is successfully reduced by the mesostructural modification of the electrode–electrolyte interface. Although small gaps between the measured and simulated data exist, the simulation results well reproduce the experimental ones because the structures of the tested cells were implemented in the numerical model we developed. Note that the gaps may be caused by an overestimation of the activation overpotential in the cathode; this is because the electrochemical reaction that occurs at LSCF–GDC–pore TPBs, which also contributes to the electrochemical performance of SOFCs [22,48], was not taken into account in the numerical model we developed. Additionally, an error associated with the contribution of gas diffusion within the anode may result in the gaps, particularly at a high current density. Although the dusty-gas model was used to analyze the gas diffusion in the electrodes in this work, whether the existing gas diffusion models [35,36,49–53] can accurately express the phenomenon of mass transport within porous electrodes remains to be clarified. Nonetheless, good agreement is achieved between the experimental and simulation results; the relative errors in a terminal voltage at the same current density are no more than 10%, which is much smaller than those reported in the literature [1,20] (500–600%). Thus, the numerical model developed in this work is feasible for further quantitative analysis. Note that the numerical model we developed is thoroughly based on the structural parameters quantified from the results of structural analysis and the physicochemical phenomena within SOFCs expressed with empirical formulas reported in the literature; that is, we carried out model validation without tuning any factors such as structural parameters, exponents in

exchange current density models, and so forth.

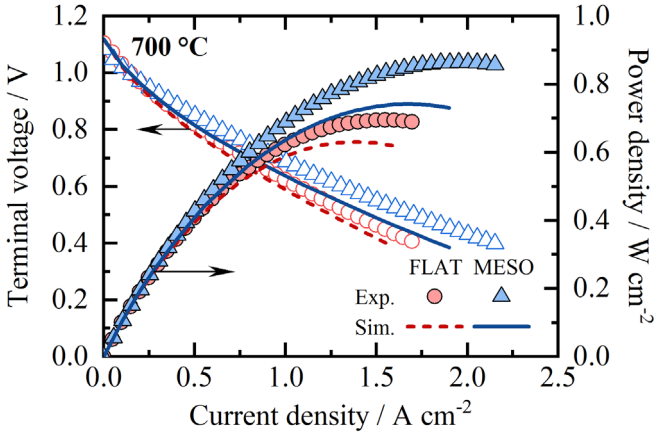

Fig. 2 *i–V* and *i–P* curves of cells obtained from experiment (plots) and numerical simulation (lines) at 700 °C.

4.2. Cell overpotential

The average values of the overpotential components in the cells at an average current density of 1.0 A cm^{-2} at 700 °C as representative operating conditions are shown in **Fig. 3**. Note that the ohmic losses due to the electron transport in each cell component on the order of 0.01 mV and the concentration overpotential in the cathode on the order of 0.1 mV are omitted from the graphs. The percentages are the changes in the overpotential components of the mesoscale-modified cell relative to the flat cell. It was found that the total overpotential in the mesoscale-modified cell (481 mV) is 9.21% (48.8 mV) smaller than that in the flat cell (530 mV). This is because all the overpotential components except for the concentration overpotential in the anode are reduced by the mesostructural modification of the electrode–electrolyte interface.

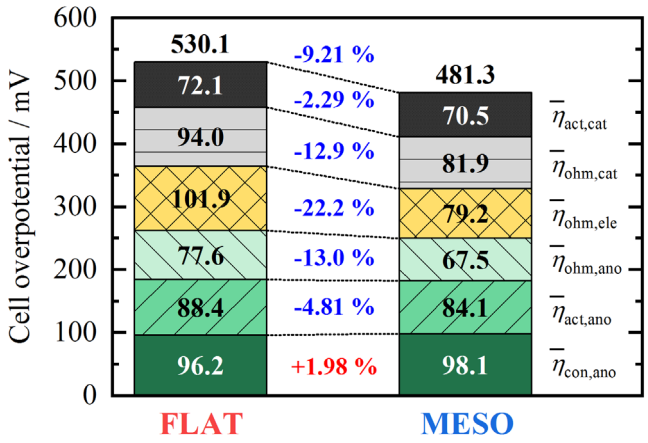

Fig. 3 Overpotential components in flat and mesoscale-modified cells at 1.0 A cm^{-2} at 700 °C and their relative changes from the mesoscale-modified cell to the flat cell.

The ohmic loss due to oxide ion transport in the electrolyte in the mesoscale-modified cell is 22.2% (22.7 mV) lower than that in the flat cell. The relative decrease in the ohmic loss RD_{ohm} can be calculated as

$$RD_{\mathrm{ohm}} = 1 - \frac{\eta_{\mathrm{ohm,MESO}}}{\eta_{\mathrm{ohm,FLAT}}}. \tag{26}$$

The right-hand side of Eq. (26) is equal to the relative decrease in Joule heating; thus, it can be re-written as

$$RD_{\mathrm{ohm}} = 1 - \frac{Q_{\mathrm{ohm,MESO}}}{Q_{\mathrm{ohm,FLAT}}}. \tag{27}$$

Here, Q_{ohm} is the Joule heating and can be expressed as

$$Q_{\mathrm{ohm}} = \iint \sigma^{-1} i^2 dxdy. \tag{28}$$

Here, we consider a situation where the same electric current is applied to both a flat cell and a mesoscale-modified cell whose electrode–electrolyte interfacial area is α times larger than that in the flat cell. Assuming that the ionic current density in the mesoscale-modified cell uniformly flows inside the electrolyte in the electrolyte thickness direction, the local ionic current density is reduced to $1/\alpha$ times that in the flat cell. If the electrolyte thickness t_{ele} is homogeneous, the Joule heating in the electrolyte in the flat cell, $Q_{\mathrm{ohm,ele,FLAT}}$, and that in the mesoscale-modified cell, $Q_{\mathrm{ohm,ele,MESO}}$, can be respectively expressed as

$$Q_{\mathrm{ohm,ele,FLAT}} = \frac{i_{\mathrm{cell}}^2}{\sigma_{\mathrm{O^{2-},YSZ}}/t_{\mathrm{ele}}} L \tag{29}$$

$$Q_{\mathrm{ohm,ele,MESO}} = \frac{(i_{\mathrm{cell}}/\alpha)^2}{\sigma_{\mathrm{O^{2-},YSZ}}/t_{\mathrm{ele}}} \alpha L. \tag{30}$$

Here, i_{cell} is the cell current density. Thus, the relative decrease in ohmic loss in the electrolyte, $RD_{\mathrm{ohm,ele}}$, can be estimated as

$$RD_{\mathrm{ohm,ele}} = 1 - \frac{1}{\alpha}. \tag{31}$$

From Eq. (31), the relative decrease in ohmic loss in the electrolyte is estimated to be 10.1% (=1−1/1.11); however, that obtained from the simulation (22.2%) is much larger than the estimate. This mismatch suggests that the assumption that the ionic current density is uniformly distributed inside an electrolyte is incorrect because of the inhomogeneous electrolyte thickness in the mesoscale-modified cell. This issue will be discussed later.

The activation overpotentials in the anode and cathode in the mesoscale-modified cell are 4.81% (4.25 mV) and 2.29% (1.65 mV) lower than those in the flat cell, respectively. The activation overpotential, which is attributed to the electrochemical reaction at the reaction sites distributed in the

electrochemically active region, is reduced owing to a decrease in the amount of electrochemical reaction per unit reaction site. This is because the area of the electrochemically active regions in both electrodes is enlarged by the mesostructural modification of the electrode–electrolyte interface [1,4,5,7–10,18,20,54]. Similarly to Eqs. (26) and (27), the relative decrease in the activation overpotential RD_{act} can be calculated as

$$RD_{\mathrm{act}} = 1 - \frac{\eta_{\mathrm{act,MESO}}}{\eta_{\mathrm{act,FLAT}}} = 1 - \frac{Q_{\mathrm{act,MESO}}}{Q_{\mathrm{act,FLAT}}}. \tag{32}$$

Here, Q_{act} is the energy loss associated with the electrochemical reaction and is expressed as

$$Q_{\mathrm{act}} = \iint \eta_{\mathrm{act}} i_{\mathrm{ct}} dxdy. \tag{33}$$

Note that when the activation overpotential η_{act} is sufficiently small (no more than around 0.1 V), the nonlinear Butler–Volmer-type equation can be approximated as [55]

$$i_{\mathrm{ct}} \cong i_0 \left[\exp\left(\frac{\beta F}{RT}\eta_{\mathrm{act}}\right) - \exp\left(-\frac{\beta F}{RT}\eta_{\mathrm{act}}\right)\right] = 2i_0 \sinh\left(\frac{\beta F}{RT}\eta_{\mathrm{act}}\right); \tag{34}$$

thus,

$$\eta_{\mathrm{act}} \cong \frac{RT}{\beta F} \sinh^{-1}\left(\frac{i_{\mathrm{ct}}}{2i_0}\right). \tag{35}$$

Here, β is a constant. In this work, to approximate Eqs. (15) and (16) with the hyperbolic sine function, constants are given as 1.5 and 1.1, respectively. Substituting Eq. (35) into Eq. (33) gives

$$Q_{\mathrm{act}} \cong \iint \frac{RT}{\beta F} \sinh^{-1}\left(\frac{i_{\mathrm{ct}}}{2i_0}\right) i_{\mathrm{ct}} dxdy. \tag{36}$$

When the electrochemical reaction uniformly occurs inside an effective reaction region with a constant thickness t_{eff} adjacent to the electrode–electrolyte interface, the following equations can be established:

$$\bar{\imath}_{\mathrm{ct,FLAT}} = \frac{i_{\mathrm{cell}}}{t_{\mathrm{eff}}} \tag{37}$$

$$\bar{\imath}_{\mathrm{ct,MESO}} = \frac{i_{\mathrm{cell}}}{\alpha t_{\mathrm{eff}}}. \tag{38}$$

Here, $\bar{\imath}_{\mathrm{ct}}$ is a uniform charge-transfer current density. Assuming that t_{eff} is sufficiently small compared with the mesostructure, the activation energy loss in the flat cell, $Q_{\mathrm{act,FLAT}}$, and that in the mesoscale-modified cell, $Q_{\mathrm{act,MESO}}$, can be respectively written as

$$Q_{\mathrm{act,FLAT}} \cong \frac{RT}{\beta F} \sinh^{-1}\left(\frac{i_{\mathrm{cell}}}{2i_0 t_{\mathrm{eff}}}\right) \times \frac{i_{\mathrm{cell}}}{t_{\mathrm{eff}}} \times L \times t_{\mathrm{eff}} \tag{39}$$

$$Q_{\mathrm{act,MESO}} \cong \frac{RT}{\beta F} \sinh^{-1}\left(\frac{i_{\mathrm{cell}}}{2i_0 \alpha t_{\mathrm{eff}}}\right) \times \frac{i_{\mathrm{cell}}}{\alpha t_{\mathrm{eff}}} \times \alpha L \times t_{\mathrm{eff}}. \tag{40}$$

Thus, the relative decrease in activation overpotential in the electrode can be estimated as

$$RD_{\mathrm{act}} = 1 - \frac{\sinh^{-1}\left(\frac{i_{\mathrm{cell}}}{2i_0 \alpha t_{\mathrm{eff}}}\right)}{\sinh^{-1}\left(\frac{i_{\mathrm{cell}}}{2i_0 t_{\mathrm{eff}}}\right)}. \tag{41}$$

According to Eq. (41), when the realistic values of 5–20 μm [11–15] are used for the thickness of the effective reaction region t_{eff}, the relative decreases in activation overpotential in the anode are

estimated to be 6.32–10.5% and those in the cathode are 6.88–7.52%. However, those obtained from the simulation (4.81% in the anode and 2.29% in the cathode) are smaller than these estimates. These mismatches may be due to the incorrect assumption that the electrochemical reaction uniformly occurs in an effective reaction region, which will also be discussed later.

The concentration overpotential in the anode in the mesoscale-modified cell is 1.98% (1.90 mV) higher than that in the flat cell. This is mainly caused by the fact that the average anode thickness in the mesoscale-modified cell is increased by about 18.1 μm compared with that in the flat cell by attaching the anode ridge structures to the surface of the anode disk; the concentration overpotential in the anode in a flat cell where the anode thickness was set at 470 μm (≈ 450+18.1 μm) was found by simulation to be 98.2 mV (not shown), which is similar to that in the mesoscale-modified cell. In addition, the increase in concentration overpotential in the anode is relatively small, suggesting that it rarely hinders the improvement in cell performance at the high hydrogen partial pressure set in this work.

4.3. Physicochemical quantities within mesoscale-modified cell

As mentioned in the previous section, the relative decreases in ohmic and activation overpotentials obtained from the simulation differ from those estimated under the assumptions that the local ionic and charge-transfer current densities are uniformly distributed inside a cell. It is presumed that the mismatches are caused by other factors such as the interfacial area enlargement and thickness inhomogeneity in the mesoscale-modified cell (see **Fig. 1(a)**). In this section, therefore, distributions of the physicochemical quantities that contribute to the electrochemical reactions in the cells are analyzed and the mismatches are quantitatively discussed on the basis of the energy losses attributed to such quantities.

4.3.1. Electrochemical potential of oxide ions

Figure 4 shows the distributions of the electrochemical potential of the oxide ions $\bar{\mu}_{O^{2-}}$ in the flat and mesoscale-modified cells at 1.0 A cm^{-2} at 700 °C, where the dotted black lines represent the electrode–electrolyte interface. It was found that the equipotential lines of the electrochemical potential of the oxide ions in the electrolyte of the mesoscale-modified cell are not parallel to the electrode–electrolyte interface; a similar trend was reported in the literature [1,6,17,18,23]. This means that the electrochemical potentials of oxide ions at points (calculation grids) located at the same distance from the electrode–electrolyte interface in the mesoscale-modified cell are not the same, unlike those in the flat cell.

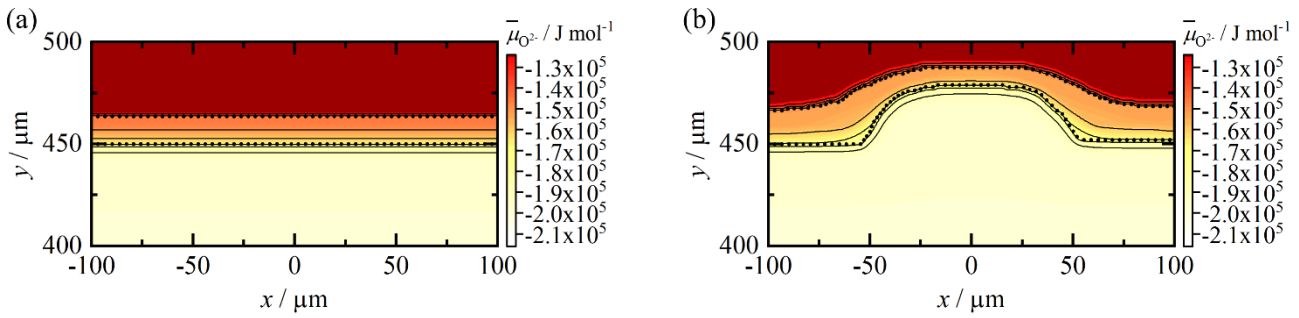

Fig. 4 Distributions of electrochemical potential of oxide ions in (a) flat and (b) mesoscale-modified cells at 1.0 A cm^{-2} at 700 °C (dotted black lines: electrode–electrolyte interface).

4.3.2. Ionic current density

Figure 5 shows the distributions of the magnitude of the ionic current density $i_{O^{2-}}$ $(= \|\mathbf{i}_{O^{2-}}\|)$ in the flat and mesoscale-modified cells at 1.0 A cm^{-2} at 700 °C. The ionic current density in the electrolyte in the mesoscale-modified cell has a nonuniform distribution, in contrast to that in the flat cell. That is, the assumption that the ionic current density is uniformly distributed inside an electrolyte is incorrect for the mesoscale-modified cell prepared in this work. Therefore, the relative decrease in ohmic loss in the electrolyte cannot be correctly expressed using Eq. (31).

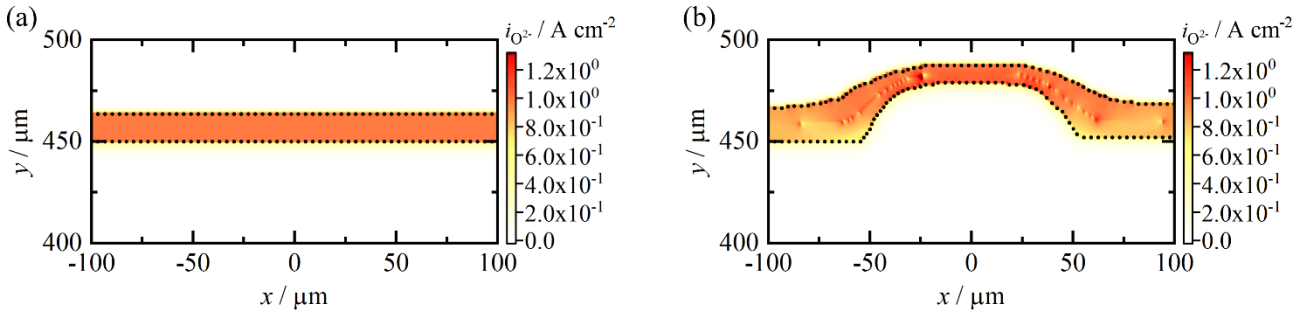

Fig. 5 Distributions of ionic current density in (a) flat and (b) mesoscale-modified cells at 1.0 A cm^{-2} at 700 °C (dotted black lines: electrode–electrolyte interface).

In the mesoscale-modified cell, the local ionic current density is higher in regions where the local electrolyte thickness is smaller, as shown in **Fig. 5(b)**. Thus, it can be inferred that not only the interfacial area enlargement but also the thickness inhomogeneity reduces the ohmic loss. From this, the relative decrease in Joule heating in the electrolyte (Eq. (27)) is expressed as the superposition of the effects of the two structural features in the mesoscale-modified cell as

$$RD_{\mathrm{ohm,ele}} = 1 - \frac{Q_{\mathrm{ohm,ele,MESO}}}{Q_{\mathrm{ohm,ele,FLAT}}} = 1 - \left(\frac{Q_{\mathrm{ohm,ele,MESO}}}{\bar{Q}_{\mathrm{ohm,ele,MESO}}}\right)\left(\frac{\bar{Q}_{\mathrm{ohm,ele,MESO}}}{Q_{\mathrm{ohm,ele,FLAT}}}\right). \tag{42}$$

Here, $\bar{Q}_{\mathrm{ohm,ele,MESO}}$ indicates the Joule heating in the electrolyte in a mesoscale-modified cell where the electrode–electrolyte interfacial area is enlarged by α compared with that in the flat cell and the electrolyte has a homogeneous thickness. Note that the first and second ratios on the rightmost-hand side of Eq. (42) correspond to the effects of the thickness inhomogeneity and interfacial area enlargement on Joule heating, respectively.

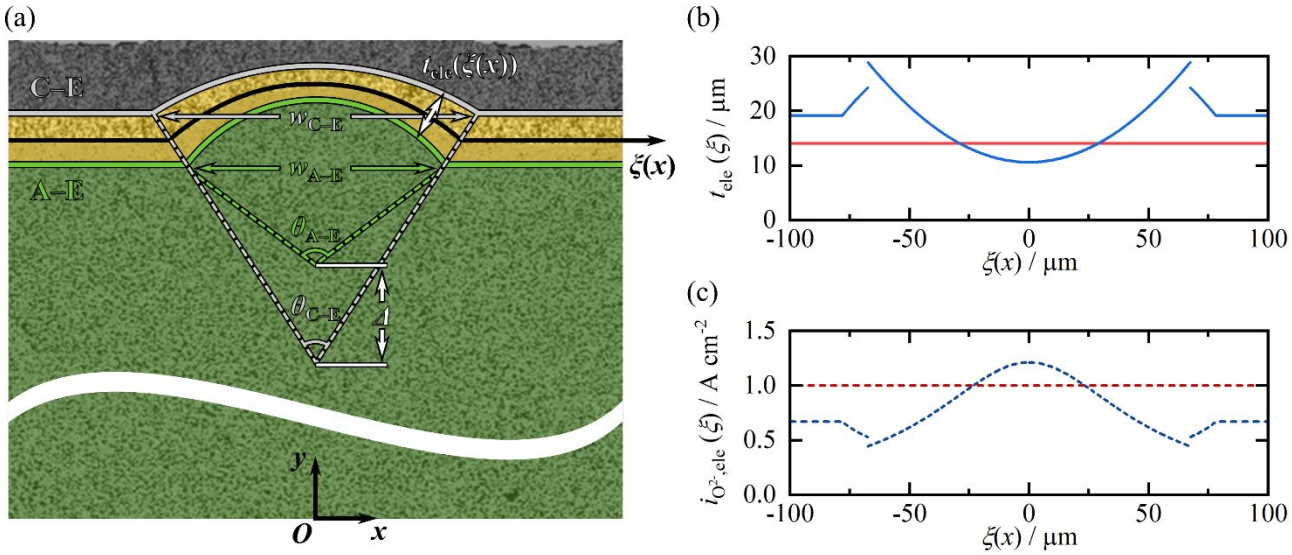

Fig. 6 (a) Approximated geometric shapes of electrode–electrolyte interface in mesoscale-modified cell based on SEM image and (b) electrolyte thickness and (c) ionic current density in electrolyte in flat and mesoscale-modified cells.

To mathematically analyze the structural effects, we model the geometric shapes of the electrode–electrolyte interface in the mesoscale-modified cell with a circular arc in the patterned area and a straight line in the nonpatterned area, as shown in **Fig. 6(a)**. In this study, the electrolyte thickness $t_{\mathrm{ele}}(\xi(x))$ is defined in the direction perpendicular to the centerline between the interfaces (ξ-axis) and is approximated as follows (further details in Appendix A):

$$t_{\mathrm{ele}}\left(\xi(x)\right) =$$

$$\begin{cases} \dfrac{w_{\mathrm{C-E}}}{2\sin\left(\frac{\theta_{\mathrm{C-E}}}{2}\right)} - \dfrac{w_{\mathrm{A-E}}}{2\sin\left(\frac{\theta_{\mathrm{A-E}}}{2}\right)} - \Delta, & x = 0 \\ \sqrt{\left(\dfrac{w_{\mathrm{C-E}}}{2\sin\left(\frac{\theta_{\mathrm{C-E}}}{2}\right)}\right)^2 - \dfrac{\left(B(x)+\frac{\Delta}{2}\right)^2}{\left(A(x)\right)^2+1}} - \sqrt{\left(\dfrac{w_{\mathrm{A-E}}}{2\sin\left(\frac{\theta_{\mathrm{A-E}}}{2}\right)}\right)^2 - \dfrac{\left(B(x)-\frac{\Delta}{2}\right)^2}{\left(A(x)\right)^2+1}} - \dfrac{A(x)\Delta}{\sqrt{\left(A(x)\right)^2+1}}, & 0 < |x| \le \dfrac{w_{\mathrm{A-E}}+w_{\mathrm{C-E}}}{4} \\ \sqrt{\left(\dfrac{w_{\mathrm{C-E}}}{2\sin\left(\frac{\theta_{\mathrm{C-E}}}{2}\right)}\right)^2 - x^2} - \dfrac{w_{\mathrm{A-E}}}{2\tan\left(\frac{\theta_{\mathrm{A-E}}}{2}\right)} - \Delta, & \dfrac{w_{\mathrm{A-E}}+w_{\mathrm{C-E}}}{4} \le |x| \le \dfrac{w_{\mathrm{C-E}}}{2} \\ \dfrac{w_{\mathrm{C-E}}}{2\tan\left(\frac{\theta_{\mathrm{C-E}}}{2}\right)} - \dfrac{w_{\mathrm{A-E}}}{2\tan\left(\frac{\theta_{\mathrm{A-E}}}{2}\right)} - \Delta, & \text{otherwise} \end{cases}. \tag{43}$$

Here, w and θ are the width of the ridge structure and the central angle of the arc, respectively. Δ indicates the distance between the centers of the arcs and can be calculated as

$$\Delta = \frac{w_{\mathrm{C-E}}}{2\sin\left(\frac{\theta_{\mathrm{C-E}}}{2}\right)} - \frac{w_{\mathrm{A-E}}}{2\sin\left(\frac{\theta_{\mathrm{A-E}}}{2}\right)} - t_{\mathrm{ele,top}}, \tag{44}$$

where $t_{\mathrm{ele,top}}$ is the electrolyte thickness at the top of the corrugated structure. $A(x)$ and $B(x)$ are respectively given as

$$A(x) = \frac{\sqrt{\left(\dfrac{w_{\mathrm{C-E}}}{2\sin\left(\frac{\theta_{\mathrm{C-E}}}{2}\right)}+\dfrac{w_{\mathrm{A-E}}}{2\sin\left(\frac{\theta_{\mathrm{A-E}}}{2}\right)}\right)^2-\Delta^2}\sqrt{\left(\dfrac{w_{\mathrm{C-E}}}{2\sin\left(\frac{\theta_{\mathrm{C-E}}}{2}\right)}+\dfrac{w_{\mathrm{A-E}}}{2\sin\left(\frac{\theta_{\mathrm{A-E}}}{2}\right)}\right)^2-\Delta^2-4x^2}}{2\left(\dfrac{w_{\mathrm{C-E}}}{2\sin\left(\frac{\theta_{\mathrm{C-E}}}{2}\right)}+\dfrac{w_{\mathrm{A-E}}}{2\sin\left(\frac{\theta_{\mathrm{A-E}}}{2}\right)}\right)x} \tag{45}$$

$$B(x) = \frac{\Delta^2}{\dfrac{w_{\mathrm{C-E}}}{2\sin\left(\frac{\theta_{\mathrm{C-E}}}{2}\right)}+\dfrac{w_{\mathrm{A-E}}}{2\sin\left(\frac{\theta_{\mathrm{A-E}}}{2}\right)}}\sqrt{\frac{1}{4}-\frac{x^2}{\left(\dfrac{w_{\mathrm{C-E}}}{2\sin\left(\frac{\theta_{\mathrm{C-E}}}{2}\right)}+\dfrac{w_{\mathrm{A-E}}}{2\sin\left(\frac{\theta_{\mathrm{A-E}}}{2}\right)}\right)^2-\Delta^2}}. \tag{46}$$

Note that the electrolyte thickness in the mesoscale-modified cell, which is represented by the blue solid line in **Fig. 6(b)**, has discontinuities at $|x| = \frac{w_{\mathrm{A\text{-}E}}+w_{\mathrm{C\text{-}E}}}{4}$ (*i.e.*, $|\xi(x)| = \frac{(\alpha-1)L}{2} + \frac{w_{\mathrm{A\text{-}E}}+w_{\mathrm{C\text{-}E}}}{4}$) because the electrode–electrolyte interface was modeled by the combination of the two different shapes.

Since an equipotential line of the electrochemical potential of oxide ions is formed at the electrode–electrolyte interface, as shown in **Fig. 4**, its difference between the interfaces $\Delta\overline{\mu}_{\mathrm{O^{2-}}}$ is constant and can be expressed as

$$\Delta\overline{\mu}_{\mathrm{O^{2-}}} = \overline{\mu}_{\mathrm{O^{2-},C\text{-}E}} - \overline{\mu}_{\mathrm{O^{2-},A\text{-}E}} = -2F\int \frac{\mathbf{i}_{\mathrm{O^{2-},ele}}}{\sigma_{\mathrm{O^{2-},YSZ}}} \cdot d\mathbf{r} = \text{constant.} \tag{47}$$

Here, $\overline{\mu}_{\mathrm{O^{2-},C\text{-}E}}$ and $\overline{\mu}_{\mathrm{O^{2-},A\text{-}E}}$ are respectively the electrochemical potentials of oxide ions at the cathode–electrolyte and anode–electrolyte interfaces, $\mathbf{i}_{\mathrm{O^{2-},ele}}$ is the ionic current density vector flowing in the electrolyte, and $d\mathbf{r}$ is an infinitesimal displacement vector. Supposing that a constant ionic current flows in the direction perpendicular to the ξ-axis direction, then

$$\int \mathbf{i}_{\mathrm{O^{2-},ele}} \cdot d\mathbf{r} = i_{\mathrm{O^{2-},ele}}\big(\xi(x)\big)t_{\mathrm{ele}}\big(\xi(x)\big) = \text{constant.} \tag{48}$$

When a mesoscale-modified cell where the electrode–electrolyte interfacial area is enlarged by α compared with that in the flat cell has an electrolyte with a homogeneous thickness of $(k/\alpha)t_{\mathrm{ele,FLAT}}$, the following equation can be established:

$$i_{\mathrm{O^{2-},ele}}\big(\xi(x)\big)t_{\mathrm{ele}}\big(\xi(x)\big) = \frac{i_{\mathrm{cell}}}{\alpha} \times \frac{k}{\alpha} t_{\mathrm{ele,FLAT}}. \tag{49}$$

Here, k is the ratio of the electrolyte volume in the mesoscale-modified cell to that in the flat cell and $t_{\mathrm{ele,FLAT}}$ is the electrolyte thickness in the flat cell. Note that the electrolyte volume in the mesoscale-

modified cell is slightly larger than that in the flat cell, as mentioned in Section 3.1, *i.e.*, the ratio of the electrolyte thickness in the mesoscale-modified cell to that in the flat cell, k/α (= 1.14/1.11 = 1.02), is greater than 1. By using the above relationship, the ionic current density in the electrolyte in the mesoscale-modified cell, which is represented by the blue dashed line in **Fig. 6(c)**, can be expressed as

$$i_{\mathrm{O^{2-}},\mathrm{ele}}\big(\xi(x)\big) = \left(\frac{i_{\mathrm{cell}}}{\alpha} \times \frac{k}{\alpha} t_{\mathrm{ele,FLAT}}\right) / t_{\mathrm{ele}}\big(\xi(x)\big). \tag{50}$$

Hence, the Joule heating in the electrolyte in the mesoscale-modified cell, $Q_{\mathrm{ohm,ele,MESO}}$, can be written as

$$Q_{\mathrm{ohm,ele,MESO}} = \int \frac{\left(i_{\mathrm{O^{2-}},\mathrm{ele}}\big(\xi(x)\big)\right)^2}{\sigma_{\mathrm{O^{2-}},\mathrm{YSZ}}} t_{\mathrm{ele}}\big(\xi(x)\big) d\xi(x) = \int \frac{\left(\frac{i_{\mathrm{cell}}}{\alpha} \times \frac{k}{\alpha} t_{\mathrm{ele,FLAT}}\right)^2}{\sigma_{\mathrm{O^{2-}},\mathrm{YSZ}} t_{\mathrm{ele}}\big(\xi(x)\big)} d\xi(x). \tag{51}$$

If the electrolyte thickness is uniform and constant at $(k/\alpha)t_{\mathrm{ele,FLAT}}$, Eq. (51) can be calculated as

$$\bar{Q}_{\mathrm{ohm,ele,MESO}} = \frac{\left(\frac{i_{\mathrm{cell}}}{\alpha}\right)^2}{\sigma_{\mathrm{O^{2-}},\mathrm{YSZ}} / \frac{k}{\alpha} t_{\mathrm{ele,FLAT}}} \alpha L. \tag{52}$$

By using the structural parameters of the mesoscale-modified cell measured using the ImageJ open-source image processing program [56], which are summarized in **Table 3**, the relative decreases in Joule heating due to the thickness inhomogeneity and interfacial area enlargement are calculated to be 18.5 and 8.21%, respectively (the Joule heating in the mesoscale-modified cell was calculated by a Riemann sum of Eq. (51) over the closed interval $\left[-\frac{L}{2}, \frac{L}{2}\right]$ using 202000 uniform subdivisions). According to Eq. (42), therefore, the Joule heating in the electrolyte is reduced by 25.2%, which is

close to the reduction obtained from the numerical simulation (22.2%). Note that the relative decreases in ohmic resistance (loss) estimated by considering the structures of the mesoscale-modified cells prepared in the literature [7] are very close to the measured values with a relative error of no more than *ca*. 5.5%.

Table 3 Average values of structural parameters of mesoscale-modified cell.

$\theta_{\mathrm{A-E}}/^{\circ}$	$\theta_{\mathrm{C-E}}/^{\circ}$	$w_{\mathrm{A-E}}/\mu\mathrm{m}$	$w_{\mathrm{C-E}}/\mu\mathrm{m}$	$\Delta/\mu\mathrm{m}$
109.3	55.3	102.4	145.5	8.4

4.3.3. Charge-transfer current density

As discussed in Section 4.2, the relative decreases in activation overpotentials (4.81% in the anode and 2.29% in the cathode) are smaller than those estimated under the assumption that the electrochemical reactions uniformly occur in the effective reaction region (6.32–10.5% in the anode and 6.88–7.52% in the cathode). This implies that the electrochemical reactions nonuniformly occur, meaning that the relative decreases in activation overpotential cannot be expressed by Eq. (41).

Considering that the total amount of the electrochemical reaction is the same for both cells ($\iint i_{\mathrm{ct}}\,dxdy = \text{constant}$) and that the form of $x\sinh^{-1}(x)$ under the integral sign of the approximated activation energy loss (Eq. (36)) is a monotonically increasing and concave upward function for all positive real numbers, the following inequalities can be established:

$$Q_{\mathrm{act,FLAT}} \cong \iint \frac{RT}{\beta F}\sinh^{-1}\left(\frac{i_{\mathrm{ct,FLAT}}}{2i_0}\right) i_{\mathrm{ct,FLAT}}\,dxdy > \frac{RT}{\beta F}\sinh^{-1}\left(\frac{i_{\mathrm{cell}}}{2i_0 t_{\mathrm{eff}}}\right) i_{\mathrm{cell}}L \tag{53}$$

$$Q_{\mathrm{act,MESO}} \cong \iint \frac{RT}{\beta F}\sinh^{-1}\left(\frac{i_{\mathrm{ct,MESO}}}{2i_0}\right) i_{\mathrm{ct,MESO}}\,dxdy > \frac{RT}{\beta F}\sinh^{-1}\left(\frac{i_{\mathrm{cell}}}{2i_0 \alpha t_{\mathrm{eff}}}\right) i_{\mathrm{cell}}L. \tag{54}$$

Details of the above inequalities are described in Appendix B. Note that the ratio of the activation energy loss obtained from the simulation to that estimated under the assumption of a uniform

electrochemical reaction increases when the nonuniformity of the distribution of the charge-transfer current density becomes stronger. Thus, the following inequality can be obtained:

$$\frac{Q_{\mathrm{act,MESO}}}{\frac{RT}{\beta F}\sinh^{-1}\left(\frac{i_{\mathrm{cell}}}{2i_0\alpha t_{\mathrm{eff}}}\right)i_{\mathrm{cell}}L} > \frac{Q_{\mathrm{act,FLAT}}}{\frac{RT}{\beta F}\sinh^{-1}\left(\frac{i_{\mathrm{cell}}}{2i_0 t_{\mathrm{eff}}}\right)i_{\mathrm{cell}}L}. \tag{55}$$

Hence,

$$RD_{\mathrm{act}} = 1 - \frac{Q_{\mathrm{act,MESO}}}{Q_{\mathrm{act,FLAT}}} < 1 - \frac{\sinh^{-1}\left(\frac{i_{\mathrm{cell}}}{2i_0\alpha t_{\mathrm{eff}}}\right)}{\sinh^{-1}\left(\frac{i_{\mathrm{cell}}}{2i_0 t_{\mathrm{eff}}}\right)}. \tag{56}$$

That is, the relative decrease in activation overpotential is smaller than that estimated under the assumption of the uniform electrochemical reaction in the effective reaction region.

From the above results, it can be concluded that the decreases in ohmic and activation overpotentials are respectively larger and smaller than those estimated under the assumptions that the ionic and charge-transfer current densities are uniformly distributed in a cell; this is mainly due to the nonuniform distributions of all physicochemical quantities that contribute to the electrochemical reactions in the mesoscale-modified cell.

4.4. Effect of distribution nonuniformity on cell performance

In this section, the effect of mesostructural modification on the electrochemical performance of anode-supported SOFCs under various current density conditions is discussed. **Figure 7** shows the decreases in the average overpotentials of the mesoscale-modified cell relative to the flat cell as a function of the current density. Note that a relative increase is represented by a negative value. The relative decrease in the total ohmic loss RD_{ohm} becomes larger with increasing current density. As described in Eq. (50), the ionic current density in the electrolyte in the mesoscale-modified cell is

inversely proportional to the electrolyte thickness; thus, the local ionic current density is higher in regions where the local electrolyte thickness is smaller. This is more prominent at a high current density, resulting in a stronger nonuniformity of the local Joule heating. Consequently, the Joule heating in the electrolyte in the mesoscale-modified cell is reduced by more than that in the flat cell at a high current density, and thereby, a large relative decrease in ohmic loss occurs. In contrast to the relative decrease in ohmic loss, the relative decreases in the activation overpotentials in the electrodes, RD_{act}, become smaller with increasing current density. This is because the right-hand side of the inequality for the relative decrease in activation energy loss (Eq. (56)) is a monotonically decreasing function with respect to the current density, resulting in only a small difference between the activation energy losses in both cells at a high current density. The relative increase in concentration overpotential in the anode $RD_{\mathrm{con,act}}$ is almost constant because it is mainly affected by the increase in average anode thickness, as mentioned in Section 4.2. The relative decrease in the total cell overpotential RD_{total} becomes larger with increasing current density, the same as the trend of the total ohmic loss. This is because the decrease in the sum of the ohmic losses in each cell component accounts for most of the total decrease in cell overpotential (*e.g.*, the ratio of the decrease in total ohmic loss with respect to the total decrease at 1.0 A cm^{-2} at 700 °C is 91.8%). From these results, it can be concluded that the effect of mesostructural modification on improving the electrochemical performance of anode-supported SOFCs is greater at a high current density.

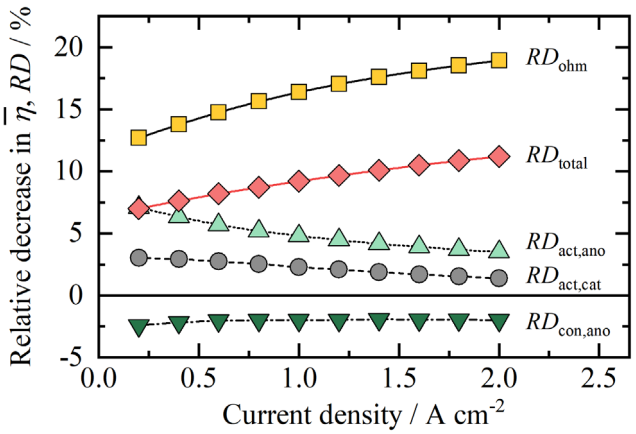

Fig. 7 Decreases in overpotential components of mesoscale-modified cell relative to flat cell at 700 °C.

5. Conclusions

We clarified the mechanism of the improved electrochemical performance of an anode-supported SOFC by the mesostructural modification of the electrode–electrolyte interface. After preparing two types of anode-supported SOFC having different electrode–electrolyte interfacial areas, we developed a 2D numerical model in which cell structures with a wide range of length scales were implemented. It was verified that simulation results well reproduced experimental results in terms of electrochemical characteristics, *i.e.*, the electrochemical performance of the mesoscale-modified cell was improved compared with that of the flat cell. It was found that the structural features in the mesoscale-modified cell, such as interfacial area enlargement and thickness inhomogeneity, caused nonuniform distributions of physicochemical quantities that contribute to electrochemical reactions. Consequently, the decreases in the ohmic and activation overpotentials of the mesoscale-modified cell relative to the flat cell were respectively larger and smaller than those estimated under the assumptions that the ionic and charge-transfer current densities in a cell have uniform distributions. Moreover, the ionic current density distribution had a strong nonuniformity at a high current density, leading to a large relative decrease in ohmic loss. On the other hand, the concentration overpotential in the anode was slightly increased, which was mainly caused by the fact that the average anode thickness was increased by attaching the anode ridge structures. However, it rarely hindered the improvement in cell performance at the high hydrogen partial pressure set in this work. Furthermore, the relative decrease in cell overpotential was larger at a high current density, indicating that the effect of mesostructural modification on improving the electrochemical performance of anode-supported SOFCs is more prominent at a high current density.

Acknowledgment

This work was partially supported by Japan Science and Technology Agency (JST) under Collaborative Research Based on Adaptable and Seamless Technology Transfer Program through Target-driven R&D (A-STEP) Grant Number JPMJTS1613. Also, this work was partially supported by the Kyoto University Nanotechnology Hub in the “Nanotechnology Platform Project”, sponsored by the Ministry of Education, Culture, Sports, Science and Technology, Japan (MEXT). Moreover, this work was partially supported by JSPS KAKENHI Grant Number 19K04216. Special thanks should be given to Mr. M. Sasaki, a former student in Thermal Engineering Laboratory of Kyoto University, who helped us improve the calculation code.

Appendix A. Electrolyte thickness in mesoscale-modified cell

This appendix describes the electrolyte thickness in the mesoscale-modified cell discussed in Section 4.3.2.

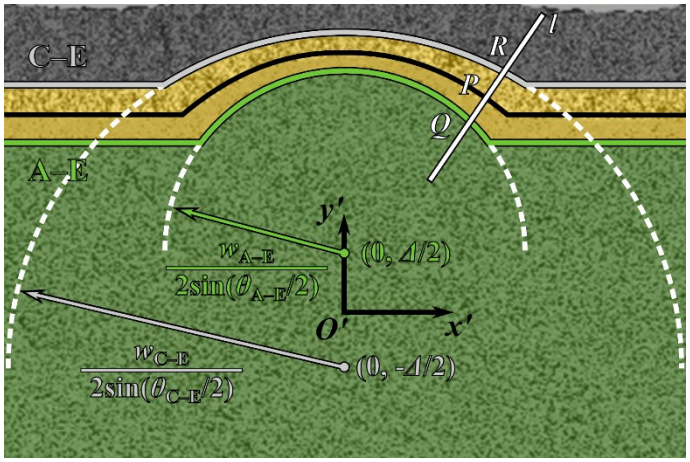

Fig. A.1 Geometric shapes of electrode–electrolyte interface in mesoscale-modified cell modeled by circular arc and straight line.

As illustrated in **Fig. A.1**, suppose that the equations of the anode–electrolyte (green solid line) and cathode–electrolyte (gray solid line) interfaces, which are defined on a closed interval $\left[-\frac{L}{2}, \frac{L}{2}\right]$, are respectively given as

$$y' = \begin{cases} \frac{\Delta}{2} + \sqrt{\left(\frac{w_{A-E}}{2\sin\left(\frac{\theta_{A-E}}{2}\right)}\right)^2 - x'^2}, & |x'| \le \frac{w_{A-E}}{2} \\ \frac{\Delta}{2} + \frac{w_{A-E}}{2\tan\left(\frac{\theta_{A-E}}{2}\right)}, & \text{otherwise} \end{cases} \tag{A.1}$$

$$y' = \begin{cases} -\frac{\Delta}{2} + \sqrt{\left(\frac{w_{C-E}}{2\sin\left(\frac{\theta_{C-E}}{2}\right)}\right)^2 - x'^2}, & |x'| \le \frac{w_{C-E}}{2} \\ -\frac{\Delta}{2} + \frac{w_{C-E}}{2\tan\left(\frac{\theta_{C-E}}{2}\right)}, & \text{otherwise} \end{cases}. \tag{A.2}$$

Then, the centerline between the interfaces is an ellipse whose minor and major axes are respectively $\sqrt{\left(\frac{w_{\mathrm{A-E}}}{2\sin\left(\frac{\theta_{\mathrm{A-E}}}{2}\right)}+\frac{w_{\mathrm{C-E}}}{2\sin\left(\frac{\theta_{\mathrm{C-E}}}{2}\right)}\right)^2-\Delta^2}$ and $\frac{w_{\mathrm{A-E}}}{2\sin\left(\frac{\theta_{\mathrm{A-E}}}{2}\right)}+\frac{w_{\mathrm{C-E}}}{2\sin\left(\frac{\theta_{\mathrm{C-E}}}{2}\right)}$ [57] when $|x'|\le\frac{w_{\mathrm{A-E}}+w_{\mathrm{C-E}}}{4}$, and a straight line otherwise. Thus, its equation can be written as

$$y'=\begin{cases}\frac{1}{2}\frac{\frac{w_{\mathrm{A-E}}}{2\sin\left(\frac{\theta_{\mathrm{A-E}}}{2}\right)}+\frac{w_{\mathrm{C-E}}}{2\sin\left(\frac{\theta_{\mathrm{C-E}}}{2}\right)}}{\sqrt{\left(\frac{w_{\mathrm{A-E}}}{2\sin\left(\frac{\theta_{\mathrm{A-E}}}{2}\right)}+\frac{w_{\mathrm{C-E}}}{2\sin\left(\frac{\theta_{\mathrm{C-E}}}{2}\right)}\right)^2-\Delta^2}}\sqrt{\left(\frac{w_{\mathrm{A-E}}}{2\sin\left(\frac{\theta_{\mathrm{A-E}}}{2}\right)}+\frac{w_{\mathrm{C-E}}}{2\sin\left(\frac{\theta_{\mathrm{C-E}}}{2}\right)}\right)^2-\Delta^2-4x'^2}, & |x'|\le\frac{w_{\mathrm{A-E}}+w_{\mathrm{C-E}}}{4}\\ \frac{1}{2}\left(\frac{w_{\mathrm{A-E}}}{2\tan\left(\frac{\theta_{\mathrm{A-E}}}{2}\right)}+\frac{w_{\mathrm{C-E}}}{2\tan\left(\frac{\theta_{\mathrm{C-E}}}{2}\right)}\right), & \text{otherwise}\end{cases}. \tag{A.3}$$

Supposing that a line l is the normal line at a given point $P(x_P',y_P')$ on the centerline between the interfaces, its equation can be expressed as

$$l:\begin{cases}y'=A(x_P')x'+B(x_P'), & 0<|x'|\le\frac{w_{\mathrm{A-E}}+w_{\mathrm{C-E}}}{4}\\ x'=x_P', & \text{otherwise}\end{cases}. \tag{A.4}$$

Here, $A(x_P')$ and $B(x_P')$ are respectively given as

$$A(x_P')=\frac{\sqrt{\left(\frac{w_{\mathrm{C-E}}}{2\sin\left(\frac{\theta_{\mathrm{C-E}}}{2}\right)}+\frac{w_{\mathrm{A-E}}}{2\sin\left(\frac{\theta_{\mathrm{A-E}}}{2}\right)}\right)^2-\Delta^2}\sqrt{\left(\frac{w_{\mathrm{C-E}}}{2\sin\left(\frac{\theta_{\mathrm{C-E}}}{2}\right)}+\frac{w_{\mathrm{A-E}}}{2\sin\left(\frac{\theta_{\mathrm{A-E}}}{2}\right)}\right)^2-\Delta^2-4x_P'^2}}{2\left(\frac{w_{\mathrm{C-E}}}{2\sin\left(\frac{\theta_{\mathrm{C-E}}}{2}\right)}+\frac{w_{\mathrm{A-E}}}{2\sin\left(\frac{\theta_{\mathrm{A-E}}}{2}\right)}\right)x_P'} \tag{A.5}$$

$$B(x_P')=\frac{\Delta^2}{\frac{w_{\mathrm{C-E}}}{2\sin\left(\frac{\theta_{\mathrm{C-E}}}{2}\right)}+\frac{w_{\mathrm{A-E}}}{2\sin\left(\frac{\theta_{\mathrm{A-E}}}{2}\right)}}\sqrt{\frac{1}{4}-\frac{x_P'^2}{\left(\frac{w_{\mathrm{C-E}}}{2\sin\left(\frac{\theta_{\mathrm{C-E}}}{2}\right)}+\frac{w_{\mathrm{A-E}}}{2\sin\left(\frac{\theta_{\mathrm{A-E}}}{2}\right)}\right)^2-\Delta^2}}. \tag{A.6}$$

If the two points $Q(x_Q', y_Q')$ and $R(x_R', y_R')$ that are respectively at the anode–electrolyte and cathode–electrolyte interfaces are on line l, their coordinates are respectively calculated as

$$x_Q' = \begin{cases} \dfrac{-A(x_P)\left(B(x_P)-\frac{\Delta}{2}\right)+\sqrt{\left((A(x_P))^2+1\right)\left(\frac{w_{\text{A-E}}}{2\sin\left(\frac{\theta_{\text{A-E}}}{2}\right)}\right)^2-\left(B(x_P)-\frac{\Delta}{2}\right)^2}}{(A(x_P))^2+1}, & 0<|x_P'|\le\frac{w_{\text{A-E}}+w_{\text{C-E}}}{4} \\ x_P', & \text{otherwise} \end{cases} \quad \text{(A.7)}$$

$$y_Q' = \begin{cases} \dfrac{\Delta}{2}+\dfrac{w_{\text{A-E}}}{2\sin\left(\frac{\theta_{\text{A-E}}}{2}\right)}, & x_P'=0 \\ A(x_P)\dfrac{-A(x_P)\left(B(x_P)-\frac{\Delta}{2}\right)+\sqrt{\left((A(x_P))^2+1\right)\left(\frac{w_{\text{A-E}}}{2\sin\left(\frac{\theta_{\text{A-E}}}{2}\right)}\right)^2-\left(B(x_P)-\frac{\Delta}{2}\right)^2}}{(A(x_P))^2+1}+B(x_P), & 0<|x_P'|\le\frac{w_{\text{A-E}}+w_{\text{C-E}}}{4} \\ \dfrac{\Delta}{2}+\dfrac{w_{\text{A-E}}}{2\tan\left(\frac{\theta_{\text{A-E}}}{2}\right)}, & \text{otherwise} \end{cases} \quad \text{(A.8)}$$

$$x_R' = \begin{cases} \dfrac{-A(x_P)\left(B(x_P)+\frac{\Delta}{2}\right)+\sqrt{\left((A(x_P))^2+1\right)\left(\frac{w_{\text{C-E}}}{2\sin\left(\frac{\theta_{\text{C-E}}}{2}\right)}\right)^2-\left(B(x_P)+\frac{\Delta}{2}\right)^2}}{(A(x_P))^2+1}, & 0<|x_P'|\le\frac{w_{\text{A-E}}+w_{\text{C-E}}}{4} \\ x_P', & \text{otherwise} \end{cases} \quad \text{(A.9)}$$

$$y_R' = \begin{cases} -\dfrac{\Delta}{2}+\dfrac{w_{\text{C-E}}}{2\sin\left(\frac{\theta_{\text{C-E}}}{2}\right)}, & x_P'=0 \\ A(x_P)\dfrac{-A(x_P)\left(B(x_P)+\frac{\Delta}{2}\right)+\sqrt{\left((A(x_P))^2+1\right)\left(\frac{w_{\text{C-E}}}{2\sin\left(\frac{\theta_{\text{C-E}}}{2}\right)}\right)^2-\left(B(x_P)+\frac{\Delta}{2}\right)^2}}{(A(x_P))^2+1}+B(x_P), & 0<|x_P'|\le\frac{w_{\text{A-E}}+w_{\text{C-E}}}{4} \\ -\dfrac{\Delta}{2}+\sqrt{\left(\frac{w_{\text{C-E}}}{2\sin\left(\frac{\theta_{\text{C-E}}}{2}\right)}\right)^2-x_P'^2}, & \frac{w_{\text{A-E}}+w_{\text{C-E}}}{4}\le|x_P'|\le\frac{w_{\text{C-E}}}{2} \\ -\dfrac{\Delta}{2}+\dfrac{w_{\text{C-E}}}{2\tan\left(\frac{\theta_{\text{C-E}}}{2}\right)}, & \text{otherwise} \end{cases} \quad \text{(A.10)}$$

Therefore, the electrolyte thickness defined in the direction perpendicular to the centerline between the interfaces corresponds to the distance between the two points $\overline{QR}$, which can be calculated as

$$\overline{QR} = \begin{cases} \frac{w_{\mathrm{C-E}}}{2\sin\left(\frac{\theta_{\mathrm{C-E}}}{2}\right)} - \frac{w_{\mathrm{A-E}}}{2\sin\left(\frac{\theta_{\mathrm{A-E}}}{2}\right)} - \Delta, & x_P{}' = 0 \\ \sqrt{\left(\frac{w_{\mathrm{C-E}}}{2\sin\left(\frac{\theta_{\mathrm{C-E}}}{2}\right)}\right)^2 - \frac{\left(B(x_P{}')+\frac{\Delta}{2}\right)^2}{\left(A(x_P{}')\right)^2+1}} - \sqrt{\left(\frac{w_{\mathrm{A-E}}}{2\sin\left(\frac{\theta_{\mathrm{A-E}}}{2}\right)}\right)^2 - \frac{\left(B(x_P{}')-\frac{\Delta}{2}\right)^2}{\left(A(x_P{}')\right)^2+1}} - \frac{A(x_P{}')\Delta}{\sqrt{\left(A(x_P{}')\right)^2+1}}, & 0 < |x_P{}'| \le \frac{w_{\mathrm{A-E}}+w_{\mathrm{C-E}}}{4} \\ \sqrt{\left(\frac{w_{\mathrm{C-E}}}{2\sin\left(\frac{\theta_{\mathrm{C-E}}}{2}\right)}\right)^2 - x_P{}'^2} - \frac{w_{\mathrm{A-E}}}{2\tan\left(\frac{\theta_{\mathrm{A-E}}}{2}\right)} - \Delta, & \frac{w_{\mathrm{A-E}}+w_{\mathrm{C-E}}}{4} \le |x_P{}'| \le \frac{w_{\mathrm{C-E}}}{2} \\ \frac{w_{\mathrm{C-E}}}{2\tan\left(\frac{\theta_{\mathrm{C-E}}}{2}\right)} - \frac{w_{\mathrm{A-E}}}{2\tan\left(\frac{\theta_{\mathrm{A-E}}}{2}\right)} - \Delta, & \text{otherwise} \end{cases}$$

. (A.11)

Appendix B. Inequality of activation energy loss

This appendix describes the inequality of the activation energy loss in the mesoscale-modified cell discussed in Section 4.3.3.

Let $f(x)$ and $g(x)$ be continuous functions satisfying the following conditions:

I. $f(x)$ and $g(x)$ are defined on a closed interval $[x_0, x_n]$.

II. $f(x)$ is a constant function.

III. The definite integrals of $f(x)$ and $g(x)$ from x_0 to x_n are the same.

Assume that $f(x_i) + f(x_{n-i}) = g(x_i) + g(x_{n-i})$ $(0 \le i \le n,\ n \ne 0)$ for all real numbers included in the given closed interval. Now, supposing that $h(x)$ defined on the closed interval is a function that is strictly increasing and concave upward (*e.g.*, $x\sinh^{-1}(x)$), the following inequality can be established [58]:

$$h\big(f(x_i)\big) + h\big(f(x_{n-i})\big) \le h\big(g(x_i)\big) + h\big(g(x_{n-i})\big) \tag{B.1}$$

with equality if and only if $f(x_i) = g(x_i)$. Then,

$$\sum_{i=0}^{n}\big[h\big(f(x_i)\big) + h\big(f(x_{n-i})\big)\big] \le \sum_{i=0}^{n}\big[h\big(g(x_i)\big) + h\big(g(x_{n-i})\big)\big]. \tag{B.2}$$

Owing to the facts that

$$\sum_{i=0}^{n} h\big(f(x_i)\big) = \sum_{i=0}^{n} h\big(f(x_{n-i})\big) \tag{B.3}$$

$$\sum_{i=0}^{n} h\big(g(x_i)\big) = \sum_{i=0}^{n} h\big(g(x_{n-i})\big), \tag{B.4}$$

the following inequality can be obtained:

$$\sum_{i=0}^{n} h\big(f(x_i)\big) \le \sum_{i=0}^{n} h\big(g(x_i)\big). \tag{B.5}$$

Multiplying both sides by $\frac{x_n - x_0}{n}$ gives

$$\sum_{i=0}^{n} h\big(f(x_i)\big)\frac{x_n - x_0}{n} \le \sum_{i=0}^{n} h\big(g(x_i)\big)\frac{x_n - x_0}{n}. \tag{B.6}$$

Taking the limit on both sides of the above inequality as n approaches infinity, we have

$$\lim_{n\to\infty} \sum_{i=0}^{n} h\big(f(x_i)\big)\frac{x_n - x_0}{n} \le \lim_{n\to\infty} \sum_{i=0}^{n} h\big(g(x_i)\big)\frac{x_n - x_0}{n}. \tag{B.7}$$

Therefore,

$$\int_{x_0}^{x_n} h\big(f(x)\big)dx \le \int_{x_0}^{x_n} h\big(g(x)\big)dx. \tag{B.8}$$

Equality holds if and only if $f(x) = g(x)$ (*i.e.*, $g(x)$ is a constant function).

Nomenclature

A_{DPB}	DPB density / $\mathrm{m^{-1}}$
$\widetilde{D}$	chemical diffusion coefficient / $\mathrm{m^2\ s^{-1}}$
D_{ij}	molecular diffusivity / $\mathrm{m^2\ s^{-1}}$
$D_{i,\mathrm{K}}$	Knudsen diffusivity / $\mathrm{m^2\ s^{-1}}$
d_i	particle/pore diameter / m
F	Faraday constant / $\mathrm{C\ mol^{-1}}$
ΔG_0	standard Gibbs free energy change / $\mathrm{J\ mol^{-1}}$
i	current density / $\mathrm{A\ m^{-2}}$
$i_{0,\mathrm{DPB}}$	exchange current density per unit DPB area / $\mathrm{A\ m^{-2}}$
$i_{0,\mathrm{TPB}}$	exchange current density per unit TPB length / $\mathrm{A\ m^{-1}}$
i_{ct}	charge-transfer current density / $\mathrm{A\ m^{-3}}$
K	permeability / $\mathrm{m^2}$
k	ratio of electrolyte volume / –
L	single repeating unit / m
l_{TPB}	TPB density / $\mathrm{m^{-2}}$
M_i	molar mass / $\mathrm{kg\ mol^{-1}}$
N_i	molar flux / $\mathrm{mol\ m^{-2}\ s^{-1}}$
P_i	partial pressure / Pa
P_{t}	total pressure / Pa
Q	energy loss / W
R	universal gas constant / $\mathrm{J\ K^{-1}\ mol^{-1}}$
RD	relative decrease / –
$(S/V)_i$	surface-to-volume ratio / $\mathrm{m^{-1}}$

$\dot{s}_i$	sink/source term for gas species / mol m^{-3} s^{-1}
T	temperature / K
t	thickness / m
t_{eff}	thickness of effective reaction region / m
V_i	volume fraction / –
V_{m}	perovskite molar volume / m^3 mol^{-1}
V_{T}	terminal voltage / V
$\sum v_i$	molecular diffusion volume / m^3 mol^{-1}
w	width of ridge structure / m
X_i	molar fraction / –

Greek symbols

α	interfacial area enlargement factor / –
Δ	distance between centers of two arcs / m
δ	oxygen nonstoichiometry / –
η	overpotential / V
θ	central angle / rad
μ	viscosity / Pa s
$\bar{\mu}_i$	electrochemical potential / J mol^{-1}
σ_i	conductivity / S m^{-1}
τ_i	tortuosity factor / –

Superscripts

bulk	value for bulk materials

eff	effective value for porous materials

Subscripts

A–E	anode–electrolyte interface
ano	anode
act	activation
C–E	cathode –electrolyte interface
cat	cathode
cell	cell
con	concentration
e^-	electronic
ele	electrolyte
FLAT	flat cell
MESO	mesoscale-modified cell
O^{2-}	oxide ionic
ohm	ohmic

References

[1] A. Konno, H. Iwai, K. Inuyama, A. Kuroyanagi, M. Saito, H. Yoshida, K. Kodani, K. Yoshikata, Mesoscale-structure control at anode/electrolyte interface in solid oxide fuel cell, J. Power Sources. 196 (2011) 98–109. doi:10.1016/j.jpowsour.2010.07.025.

[2] A. Larrea, D. Sola, M.A. Laguna-Bercero, J.I. Peña, R.I. Merino, V.M. Orera, Self-supporting thin yttria-stabilised zirconia electrolytes for solid oxide fuel cells prepared by laser machining, J. Electrochem. Soc. 158 (2011) B1193–B1197. doi:10.1149/1.3619759.

[3] Y. Xu, F. Tsumori, H. Miura, T. Osada, Improvement of solid oxide fuel cell by imprinted micropatterns on electrolyte, Micro Nano Lett. 8 (2013) 571–574. doi:10.1049/mnl.2013.0310.

[4] G. Cai, Y. Gu, L. Ge, Y. Zhang, H. Chen, L. Guo, Modification of electrolyte surface with "windows" and "dimples array" structure for SOFC based on YSZ electrolyte, Ceram. Int. 43 (2017) 8944–8950. doi:10.1016/j.ceramint.2017.04.033.

[5] J.A. Cebollero, R. Lahoz, M.A. Laguna-Bercero, A. Larrea, Tailoring the electrode-electrolyte interface of solid oxide fuel cells (SOFC) by laser micro-patterning to improve their electrochemical performance, J. Power Sources. 360 (2017) 336–344. doi:10.1016/j.jpowsour.2017.05.106.

[6] T. Shimura, K. Nagato, N. Shikazono, Evaluation of electrochemical performance of solid-oxide fuel cell anode with pillar-based electrolyte structures, Int. J. Hydrogen Energy. 44 (2019) 12043–12056. doi:10.1016/j.ijhydene.2019.03.112.

[7] H. Seo, H. Iwai, M. Kishimoto, C. Ding, M. Saito, H. Yoshida, Microextrusion printing for increasing electrode–electrolyte interface in anode-supported solid oxide fuel cells, J. Power Sources. 450 (2020) 227682. doi:10.1016/j.jpowsour.2019.227682.

[8] S.S. Shin, J.H. Kim, K.T. Bae, K.-T. Lee, S.M. Kim, J.-W. Son, M. Choi, H. Kim, Multiscale structured low-temperature solid oxide fuel cells with 13 W power at 500 °C, Energy Environ. Sci. 13 (2020) 3459–3468. doi:10.1039/D0EE00870B.

[9] A. Pesce, A. Hornés, M. Núñez, A. Morata, M. Torrell, A. Tarancón, 3D printing the next generation of enhanced solid oxide fuel and electrolysis cells, J. Mater. Chem. A. 8 (2020) 16926–16932. doi:10.1039/D0TA02803G.

[10] C. Lee, S.S. Shin, J. Choi, J. Kim, J.-W. Son, M. Choi, H.H. Shin, A micro-patterned electrode/electrolyte interface fabricated by soft-lithography for facile oxygen reduction in solid oxide fuel cells, J. Mater. Chem. A. 8 (2020) 16534–16541. doi:10.1039/D0TA03997G.

[11] M. Brown, S. Primdahl, M. Mogensen, Structure/performance relations for Ni/yttria-stabilized zirconia anodes for solid oxide fuel cells, J. Electrochem. Soc. 147 (2000) 475–485. doi:10.1149/1.1393220.

[12] K. Chen, X. Chen, Z. Lü, N. Ai, X. Huang, W. Su, Performance of an anode-supported SOFC with anode functional layers, Electrochim. Acta. 53 (2008) 7825–7830. doi:10.1016/J.ELECTACTA.2008.05.063.

[13] K. Yuan, Y. Ji, J.N. Chung, Physics-based modeling of a low-temperature solid oxide fuel cell with consideration of microstructure and interfacial effects, J. Power Sources. 194 (2009) 908–919. doi:10.1016/J.JPOWSOUR.2009.05.045.

[14] A. Konno, H. Iwai, M. Saito, H. Yoshida, Effect of characteristic lengths of electron, ion, and gas diffusion on electrode performance and electrochemical reaction area in a solid oxide fuel cell, Heat Transf. Res. 41 (2012) 700–718. doi:10.1002/htj.20373.

[15] M. Kishimoto, H. Iwai, M. Saito, H. Yoshida, Characteristic length of oxide-ion conduction for prediction of active thickness in SOFC anode, ECS Trans. 57 (2013) 2515–2525. doi:10.1149/05701.2515ecst.

[16] Y. Zhang, G. Cai, Y. Gu, L. Ge, Y. Zheng, H. Chen, L. Guo, Modifying the electrode-electrolyte interface of anode supported solid oxide fuel cells (SOFCs) by laser-machining, Energy Convers. Manag. 171 (2018) 1030–1037. doi:10.1016/j.enconman.2018.06.044.

[17] H. Iwai, A. Kuroyanagi, M. Saito, A. Konno, H. Yoshida, T. Yamada, S. Nishiwaki, Power

generation enhancement of solid oxide fuel cell by cathode–electrolyte interface modification in mesoscale assisted by level set-based optimization calculation, J. Power Sources. 196 (2011) 3485–3495. doi:10.1016/j.jpowsour.2010.12.024.

[18] A. Konno, H. Iwai, M. Saito, H. Yoshida, A corrugated mesoscale structure on electrode–electrolyte interface for enhancing cell performance in anode-supported SOFC, J. Power Sources. 196 (2011) 7442–7449. doi:10.1016/j.jpowsour.2011.04.051.

[19] A. Bertei, F. Tariq, V. Yufit, E. Ruiz-Trejo, N.P. Brandon, Guidelines for the rational design and engineering of 3D manufactured solid oxide fuel cell composite electrodes, J. Electrochem. Soc. 164 (2017) F89–F98. doi:10.1149/2.0501702jes.

[20] A. Chesnaud, F. Delloro, M. Geagea, A.-P. Abellard, J. Ouyang, D. Li, T. Shi, B. Chi, R. Ihringer, M. Cassir, A. Thorel, Corrugated electrode/electrolyte interfaces in SOFC: Theoretical and experimental development, ECS Trans. 78 (2017) 1851–1863. doi:10.1149/07801.1851ecst.

[21] C.-C. Chueh, A. Bertei, C. Nicolella, Design guidelines for the manufacturing of the electrode-electrolyte interface of solid oxide fuel cells, J. Power Sources. 437 (2019) 226888. doi:10.1016/j.jpowsour.2019.226888.

[22] A. He, T. Shimura, J. Gong, N. Shikazono, Numerical simulation of $La_{0.6}Sr_{0.4}Co_{0.2}Fe_{0.8}O_3$-$Gd_{0.1}Ce_{0.9}O_{1.95}$ composite cathodes with micro pillars, Int. J. Hydrogen Energy. 44 (2019) 6871–6885. doi:10.1016/J.IJHYDENE.2019.01.171.

[23] A. He, J. Onishi, N. Shikazono, Optimization of electrode-electrolyte interface structure for solid oxide fuel cell cathode, J. Power Sources. 449 (2020) 227565. doi:10.1016/J.JPOWSOUR.2019.227565.

[24] H. Seo, M. Kishimoto, C. Ding, H. Iwai, M. Saito, H. Yoshida, Improvement in the electrochemical performance of anode-supported solid oxide fuel cells by meso- and nanoscale structural modifications, Fuel Cells. 20 (2020) 570–579. doi:10.1002/fuce.202000079.

[25] M. Kishimoto, S. Kishida, H. Seo, H. Iwai, H. Yoshida, Prediction of electrochemical

characteristics of practical-size solid oxide fuel cells based on database of unit cell performance, Appl. Energy. 283 (2020) 116305. doi:10.1016/j.apenergy.2020.116305.

[26] H. Iwai, N. Shikazono, T. Matsui, H. Teshima, M. Kishimoto, R. Kishida, D. Hayashi, K. Matsuzaki, D. Kanno, M. Saito, H. Muroyama, K. Eguchi, N. Kasagi, H. Yoshida, Quantification of SOFC anode microstructure based on dual beam FIB-SEM technique, J. Power Sources. 195 (2010) 955–961. doi:10.1016/j.jpowsour.2009.09.005.

[27] M. Kishimoto, H. Iwai, M. Saito, H. Yoshida, Quantitative evaluation of solid oxide fuel cell porous anode microstructure based on focused ion beam and scanning electron microscope technique and prediction of anode overpotentials, J. Power Sources. 196 (2011) 4555–4563. doi:10.1016/J.JPOWSOUR.2010.12.100.

[28] M. Kishimoto, H. Iwai, M. Saito, H. Yoshida, Three-dimensional simulation of SOFC anode polarization characteristics based on sub-grid scale modeling of microstructure, J. Electrochem. Soc. 159 (2012) B315–B323. doi:10.1149/2.086203jes.

[29] M. Kishimoto, M. Lomberg, E. Ruiz-Trejo, N.P. Brandon, Enhanced triple-phase boundary density in infiltrated electrodes for solid oxide fuel cells demonstrated by high-resolution tomography, J. Power Sources. 266 (2014) 291–295. doi:10.1016/J.JPOWSOUR.2014.05.038.

[30] K. Miyoshi, T. Miyamae, H. Iwai, M. Saito, M. Kishimoto, H. Yoshida, Exchange current model for $(La_{0.8}Sr_{0.2})_{0.95}MnO_3$ (LSM) porous cathode for solid oxide fuel cells, J. Power Sources. 315 (2016) 63–69. doi:10.1016/J.JPOWSOUR.2016.02.076.

[31] B. Steele, Appraisal of $Ce_{1-y}Gd_yO_{2-y/2}$ electrolytes for IT-SOFC operation at 500°C, Solid State Ionics. 129 (2000) 95–110. doi:10.1016/S0167-2738(99)00319-7.

[32] E.D. Wachsman, K.T. Lee, Lowering the temperature of solid oxide fuel cells, Science. 334 (2011) 935–939. doi:10.1126/science.1204090.

[33] R.B. Evans, G.M. Watson, E.A. Mason, Gaseous diffusion in porous media at uniform pressure, J. Chem. Phys. 35 (1961) 2076–2083. doi:10.1063/1.1732211.

[34] R.B. Evans, G.M. Watson, E.A. Mason, Gaseous diffusion in porous media. II. Effect of pressure gradients, J. Chem. Phys. 36 (1962) 1894–1902. doi:10.1063/1.1701287.

[35] D. Arnošt, P. Schneider, Dynamic transport of multicomponent mixtures of gases in porous solids, Chem. Eng. J. Biochem. Eng. J. 57 (1995) 91–99. doi:10.1016/0923-0467(94)02900-8.

[36] M. García-Camprubí, N. Fueyo, Mass transfer in hydrogen-fed anode-supported SOFCs, Int. J. Hydrogen Energy. 35 (2010) 11551–11560. doi:10.1016/j.ijhydene.2010.04.085.

[37] H.J.M. Bouwmeester, M.W. Den Otter, B.A. Boukamp, Oxygen transport in $La_{0.6}Sr_{0.4}Co_{1-y}Fe_yO_{3-\delta}$, J. Solid State Electrochem. 8 (2004) 599–605. doi:10.1007/s10008-003-0488-3.

[38] K. Matsuzaki, N. Shikazono, N. Kasagi, Three-dimensional numerical analysis of mixed ionic and electronic conducting cathode reconstructed by focused ion beam scanning electron microscope, J. Power Sources. 196 (2011) 3073–3082. doi:10.1016/j.jpowsour.2010.11.142.

[39] U. Anselmi-Tamburini, G. Chiodelli, M. Arimondi, F. Maglia, G. Spinolo, Z.. Munir, Electrical properties of Ni/YSZ cermets obtained through combustion synthesis, Solid State Ionics. 110 (1998) 35–43. doi:10.1016/S0167-2738(98)00115-5.

[40] N.F. Bessette, W.J. Wepfer, J. Winnick, A mathematical model of a solid oxide fuel cell, J. Electrochem. Soc. 142 (1995) 3792–3800. doi:10.1149/1.2048415.

[41] E.N. Fuller, P.D. Schettler, J.C. Giddings, New method for prediction of binary gas-phase diffusion coefficients, Ind. Eng. Chem. 58 (1966) 18–27. doi:10.1021/ie50677a007.

[42] K. Yashiro, I. Nakano, M. Kuhn, S. Hashimoto, K. Sato, J. Mizusaki, Electrical conductivity and oxygen diffusivity of perovskite-type solid solution $La_{0.6}Sr_{0.4}Co_{1-y}Fe_yO_{3-\delta}$ (y=0.2, 0.4, 0.5, 0.6, 0.8), ECS Trans. 35 (2011) 1899–1907. doi:10.1149/1.3570179.

[43] T. Kawada, N. Sakai, H. Yokokawa, M. Dokiya, M. Mori, T. Iwata, Characteristics of slurry-coated nickel zirconia cermet anodes for solid oxide fuel cells, J. Electrochem. Soc. 137 (1990) 3042–3047. doi:10.1149/1.2086156.

[44] D. Kanno, N. Shikazono, N. Takagi, K. Matsuzaki, N. Kasagi, Evaluation of SOFC anode polarization simulation using three-dimensional microstructures reconstructed by FIB tomography, Electrochim. Acta. 56 (2011) 4015–4021. doi:10.1016/J.ELECTACTA.2011.02.010.

[45] A. Esquirol, N.P. Brandon, J.A. Kilner, M. Mogensen, Electrochemical characterization of $La_{0.6}Sr_{0.4}Co_{0.2}Fe_{0.8}O_3$ cathodes for intermediate-temperature SOFCs, J. Electrochem. Soc. 151 (2004) A1847–A1855. doi:10.1149/1.1799391.

[46] K. Miyoshi, H. Iwai, M. Kishimoto, M. Saito, H. Yoshida, Chromium poisoning in (La,Sr)MnO_3 cathode: Three-dimensional simulation of a solid oxide fuel cell, J. Power Sources. 326 (2016) 331–340. doi:10.1016/j.jpowsour.2016.06.110.

[47] K. Miyawaki, M. Kishimoto, H. Iwai, M. Saito, H. Yoshida, Comprehensive understanding of the active thickness in solid oxide fuel cell anodes using experimental, numerical and semi-analytical approach, J. Power Sources. 267 (2014) 503–514. doi:10.1016/j.jpowsour.2014.05.112.

[48] Y.T. Kim, Z. Jiao, N. Shikazono, Evaluation of $La_{0.6}Sr_{0.4}Co_{0.2}Fe_{0.8}O_3$-$Gd_{0.1}Ce_{0.9}O_{1.95}$ composite cathode with three dimensional microstructure reconstruction, J. Power Sources. 342 (2017) 787–795. doi:10.1016/j.jpowsour.2016.12.113.

[49] J.W. Veldsink, R.M.J. van Damme, G.F. Versteeg, W.P.M. van Swaaij, The use of the dusty-gas model for the description of mass transport with chemical reaction in porous media, Chem. Eng. J. Biochem. Eng. J. 57 (1995) 115–125. doi:10.1016/0923-0467(94)02929-6.

[50] S.B. Adler, J.A. Lane, B.C.H. Steele, Electrode kinetics of porous mixed-conducting oxygen electrodes, J. Electrochem. Soc. 143 (1996) 3554–3564. doi:10.1149/1.1837252.

[51] R. Krishna, J.A. Wesselingh, The Maxwell-Stefan approach to mass transfer, Chem. Eng. Sci. 52 (1997) 861–911. doi:10.1016/S0009-2509(96)00458-7.

[52] R. Suwanwarangkul, E. Croiset, M.W. Fowler, P.L. Douglas, E. Entchev, M.A. Douglas,

Performance comparison of Fick's, dusty-gas and Stefan–Maxwell models to predict the concentration overpotential of a SOFC anode, J. Power Sources. 122 (2003) 9–18. doi:10.1016/S0378-7753(02)00724-3.

[53] K. Tseronis, I.K. Kookos, C. Theodoropoulos, Modelling mass transport in solid oxide fuel cell anodes: a case for a multidimensional dusty gas-based model, Chem. Eng. Sci. 63 (2008) 5626–5638. doi:10.1016/j.ces.2008.07.037.

[54] A. Cubero, J.I. Peña, M.A. Laguna-Bercero, Optimization of Ni–YSZ solid oxide fuel cell anodes by surface laser melting, Appl. Surf. Sci. 335 (2015) 39–43. doi:10.1016/j.apsusc.2015.01.230.

[55] H. Onaka, H. Iwai, M. Kishimoto, M. Saito, H. Yoshida, G. Brus, J.S. Szmyd, Charge-transfer distribution model applicable to stack simulation of solid oxide fuel cells, Heat Mass Transf. 54 (2018) 2425–2432. doi:10.1007/s00231-017-2095-3.

[56] C.A. Schneider, W.S. Rasband, K.W. Eliceiri, Historical commentary NIH Image to ImageJ : 25 years of image analysis, Nat. Methods. 9 (2012) 671–675. doi:10.1038/nmeth.2089.

[57] C.S. Ogilvy, Excursions in Geometry, Dover Publications, 1990.

[58] J.L.W. V Jensen, Sur les fonctions convexes et les inégalités entre les valeurs moyennes, Acta Math. 30 (1906) 175–193. doi:10.1007/BF02418571.